

DISSECTING THE RED SEQUENCE—II. STAR FORMATION HISTORIES OF EARLY-TYPE GALAXIES  
THROUGHOUT THE FUNDAMENTAL PLANEGENEVIEVE J. GRAVES<sup>1</sup>, S. M. FABER<sup>1</sup>, & RICARDO P. SCHIAVON<sup>2</sup>*Draft version February 21, 2024*

## ABSTRACT

This analysis uses spectra of  $\sim 16,000$  nearby SDSS quiescent galaxies to track variations in galaxy star formation histories along and perpendicular to the Fundamental Plane (FP). We sort galaxies by their FP properties ( $\sigma$ ,  $R_e$ , and  $I_e$ ) and construct high  $S/N$  mean galaxy spectra that span the breadth and thickness of the FP. From these spectra, we determine mean luminosity-weighted ages,  $[\text{Fe}/\text{H}]$ ,  $[\text{Mg}/\text{H}]$ , and  $[\text{Mg}/\text{Fe}]$  based on single stellar population models using the method described in Graves & Schiavon (2008). In agreement with previous work, the star formation histories of early-type galaxies are found to form a two-parameter family. The major trend is that mean age,  $[\text{Fe}/\text{H}]$ ,  $[\text{Mg}/\text{H}]$ , and  $[\text{Mg}/\text{Fe}]$  all increase with  $\sigma$ . However, no stellar population property shows any dependence on  $R_e$  at fixed  $\sigma$ , suggesting that  $\sigma$  and not dynamical mass ( $M_{\text{dyn}} \propto \sigma^2 R_e$ ) is the better predictor of past star formation history. In addition to the main trend with  $\sigma$ , galaxies also show a range of population properties at fixed  $\sigma$  that are strongly correlated with surface brightness residuals from the FP ( $\Delta \log I_e$ ), such that higher surface brightness galaxies have younger mean ages, higher  $[\text{Fe}/\text{H}]$ , higher  $[\text{Mg}/\text{H}]$ , and lower  $[\text{Mg}/\text{Fe}]$  than lower-surface brightness galaxies. These latter trends are a major new constraint on star-formation histories.

*Subject headings:* galaxies: abundances, galaxies: elliptical and lenticular

## 1. INTRODUCTION

Early-type galaxies are known to comprise a two-parameter family in galaxy structure. In the three-dimensional (3-D) parameter space of central stellar velocity dispersion ( $\sigma$ ), galaxy effective radius ( $R_e$ ), and mean central surface brightness ( $I_e$ ), early type galaxies occupy a 2-D plane, known as the Fundamental Plane (FP; Faber et al. 1987; Dressler et al. 1987; Djorgovski & Davis 1987). The FP is relatively constant throughout the local universe (Jørgensen et al. 1996). There may be some variation with environment (Bernardi et al. 2003a), consistent with the FP in dense environments being offset toward lower  $I_e$  than the FP in the field.

There is clear evolution in the FP with redshift, which is often interpreted as evolution in the stellar mass-to-light ratio ( $M/L$ ). For field galaxies, most authors find consistent results, with  $M/L$  evolution of  $d \log(M/L_B)/dz \sim -0.7$  (Treu et al. 2005b, and references therein). Treu et al. (2005b) also find increased scatter in the FP at higher redshift, with most evolution seen in the low-mass end; while the high-mass FP appears nearly unchanged since  $z \sim 1$  other than expected passive evolution in  $M/L$ , low-mass galaxies are still “settling” onto the FP since  $z \sim 1$  (van der Wel et al. 2004; Treu et al. 2005a,b; van der Wel et al. 2005).

The local FP should then be expected to include at least some galaxies that are relatively recent arrivals. This is supported by the results of Forbes et al. (1998) and Terlevich & Forbes (2002), who find that residuals from the FP correlate with age such that galaxies offset to higher (lower) surface brightness have younger (older) ages than those occupying the FP. The thickness of the FP may therefore be an age sequence, with the most re-

cent arrivals lying at higher surface brightness than the midplane. This thickness may reveal a (narrow) third dimension to the structural parameters of early-type galaxies.

In contrast to the 2-D structural space occupied by early-type galaxies, most studies of their stellar populations have stressed only a 1-D space. Many previous authors have presented correlations between detailed stellar population properties and various measures of galaxy “size”, including  $\sigma$  (e.g., Trager et al. 2000; Thomas et al. 2005; Nelan et al. 2005; Smith et al. 2007a), stellar mass  $M_*$  (e.g., Gallazzi et al. 2005), and luminosity ( $L$ ) (e.g., Kuntschner & Davies 1998; Terlevich & Forbes 2002). However, considerable evidence suggests that early-type galaxy star formation histories in fact comprise a two parameter family. Worthey et al. (1995) demonstrated an anti-correlation between age and metallicity among galaxies with similar  $\sigma$  and showed that it helped explain the narrowness of the color- $\sigma$  and FP relations. Trager et al. (2000) quantified this anti-correlation, which they termed the “metallicity hyperplane.” The anti-correlation has been corroborated recently by Smith et al. (2008b). Thomas et al. (2005) also found a range of ages for galaxies at fixed  $\sigma$  although with no associated metallicity variation.

This is the second paper in a four-part series which demonstrates conclusively that early-type galaxies do span a 2-D space in stellar population properties, implying that their star formation histories must also occupy a two-parameter space. The goal of this series is to connect stellar population properties of early-type galaxies to their structural parameters in order to understand how galaxy structural evolution and mass assembly are related to star formation. In Graves et al. (2009, hereafter Paper I), we explored the variations in stellar populations along the color-magnitude relation of early-type

<sup>1</sup> UCO/Lick Observatory, Department of Astronomy and Astrophysics, University of California, Santa Cruz, CA 95064

<sup>2</sup> Gemini Observatory, 670 N. A’ohoku Place, Hilo, HI 96720

galaxies and showed that galaxy stellar populations not only vary systematically with  $\sigma$ , but also vary with residuals from the  $\sigma$ – $L$  relation.

In this paper, we continue that approach but map out stellar populations along and through the FP rather than the  $\sigma$ – $L$  relation. The result is to parameterize the 2-D space of stellar population variables in terms of the FP variables  $\sigma$ ,  $R_e$ , and  $I_e$ . Briefly looking forward, Paper III presents a clear parameterization of the 2-D family of early-type galaxy star formation histories and interprets the observed stellar population results as differences in the onset epoch and duration of star formation in galaxies. Paper IV compares various stellar ( $M_*/L$ ) and dynamical ( $M_{dyn}/L$ ) mass-to-light ratios for the sample galaxies and demonstrates that the observed stellar population effects are not adequate to explain the variation in  $M_{dyn}/L$  along or perpendicular to the FP.

The paper is organized as follows. Section 2 briefly reviews the selection criteria used to identify the early-type galaxy sample for this series of papers. In §3, we divide up the FP into bins of similar galaxies, stack the spectra to obtain high  $S/N$  mean spectra for each point in FP-space, and compare the spectra to models in order to determine the mean stellar population properties along and through the FP. Section 4 presents these results. A major new result is that stellar populations, and therefore galaxy star formation histories, appear to be independent of  $R_e$ , at fixed  $\sigma$ . Section 5 briefly discusses some possible explanations for why galaxy star formation histories do not depend on  $R_e$  at fixed  $\sigma$ . Finally, §6 summarizes our conclusions.

## 2. SAMPLE SELECTION

The sample of galaxies used in this work is identical to that of Paper I. A brief summary of the sample selection is included here. The sample consists of  $\sim 16,000$  galaxies from the Sloan Digital Sky Survey (SDSS; York et al. 2000) spectroscopic Main Galaxy Survey (Strauss et al. 2002) Data Release 6 (DR6; Adelman-McCarthy 2008). Galaxies are chosen from a limited redshift range ( $0.04 < z < 0.08$ ) and are selected to be quiescent galaxies based on the following criteria:

1. Galaxies have no detected emission in either the H $\alpha$  or [OII] $\lambda 3727$  lines.
2. Galaxies have centrally concentrated light profiles, as determined by the ratio of the Petrosian radii that enclose 90% and 50% of the total galaxy light ( $R_{90}/R_{50} > 2.5$  in the  $i$ -band).
3. The likelihood of a de Vaucouleurs light profile fit is at least 1.03 times larger than the likelihood of an exponential light profile fit.

Paper I showed that, although no explicit color selection has been applied, these criteria define a sample of galaxies that populate the red sequence in the color-magnitude diagram, with very few color outliers (see Figure 1 of Paper I). Remaining color outliers are excluded from this analysis, as described in §3.

By requiring the sample galaxies to have no detectable emission, we remove four types of galaxies from the sample: actively star-forming galaxies, Seyfert hosts, low ionization nuclear emission-line region (LINER) hosts, and

so-called “transition objects” (TOs) whose spectra contain emission from both star-formation and active galactic nuclei (AGN). In galaxies with ongoing active star-formation (star-forming galaxies and TOs), a small fraction of very young stars contribute disproportionately to the integrated light of the galaxy. These galaxies will therefore have significantly lower  $M_*/L$  than quiescent galaxies of comparable mass, which will change their location in FP space. These galaxies constitute about 11% of morphologically-selected early type galaxies (Schawinski et al. 2007). Excluding these galaxies removes the “youngest” early type galaxies from the sample, leaving a sample of galaxies whose  $M/L$  values and positions in FP space are not strongly biased by a small sub-population of very young stars.

Removing galaxies with emission due to AGN activity (i.e., Seyferts and LINERs) is a less obvious choice, as these galaxies likely lack the very young stars that bias  $M/L$  estimates in actively star-forming galaxies. However, host galaxies of strong AGN have stellar light profiles intermediate between early-type and late-type galaxies (Kauffmann et al. 2003), as indicated by values of  $R_{90}/R_{50}$ . Furthermore, there is evidence that these galaxies have systematically different stellar populations from quiescent early type galaxies of the same mass, with both Seyferts (Kauffmann et al. 2003) and LINERs (Graves et al. 2007) showing younger stellar population ages. In light of these differences, we defer a FP analysis of these galaxies to future work.

Defined in this way, the galaxy sample presented here contains bulge-dominated galaxies, some of which harbor significant disk components. Figure 2 in Paper I shows a selection of the sample galaxies illustrating this. Classical bulges of disk galaxies are known to lie on the FP defined by early-type galaxies (Fisher & Drory 2008; Kormendy & Fisher 2008) and are therefore relevant to this study. Because the SDSS images are fairly low-resolution, high quality automated bulge-disk decompositions are challenging. Assessing the quality of the decompositions and interpreting the output is a complicated topic and beyond the scope of the analysis presented here. We are engaged in ongoing work to assess and compare automated bulge-disk compositions with by-eye morphologies (Cheng et al., in preparation). We then intend to revisit the topic of morphological variation among quiescent galaxies and its effect on the FP and stellar population.

The FP explored in this work is defined by the galaxy central velocity dispersion ( $\sigma$ ), galaxy effective radius ( $R_e$ ), and galaxy effective surface brightness ( $I_e$ ). Following Jørgensen et al. (1996, 2006), values of  $R_e$  are derived using  $r^{1/4}$  de Vaucouleurs fits to the galaxy light profiles (i.e., Sérsic 1968 fits with  $n = 4$ ). It is likely that not all sample galaxies will have true Sérsic  $n = 4$  profiles and that this will affect the derived FP correlations. However, it is not clear that a physically meaningful comparison can be made between values of  $R_e$  derived from fitting profiles with different shapes. A separate study of the FP relationships presented here as a function of Sérsic  $n$  will be included in the FP morphology-dependence study discussed above.

In this work, velocity dispersions are taken from the SDSS DR6 catalog and corrected to a “central”  $\frac{1}{8}R_e$

aperture (see Paper I for details). Effective radii are from  $r$ -band de Vaucouleurs fits to the galaxy light profiles, converted to physical units using standard  $\Lambda$ CDM cosmology with  $\Omega_\Lambda = 0.7$ ,  $\Omega_M = 0.3$ , and  $h_0 = 0.70$ . Surface brightnesses are computed in the Johnson  $V$  band as  $I_e = L_V/2\pi R_e^2$ , where  $L_V$  is the total  $V$  band luminosity of the galaxy from a de Vaucouleurs fit to the light profile. The  $K$ -correction from observed SDSS *ugriz* photometry to rest-frame  $V$ -band is performed using the IDL code *kcorrect* v4.1.4 (Blanton et al. 2003). The de Vaucouleurs radii and luminosities are corrected for known problems with sky-subtraction around bright galaxies in the SDSS photometric pipeline, as described in Paper I. Luminosities are also corrected for Galactic extinction using the extinction values from the SDSS photometric pipeline.

The data used to identify the sample and to compute  $\sigma$ ,  $R_e$ , and  $I_e$  for each galaxy include the following parameters from the NYU Value-Added Catalog (Blanton et al. 2005) version of the SDSS DR4 (Adelman-McCarthy et al. 2006): redshift ( $z$ ), de Vaucouleurs photometry in the *ugriz* bands, and Petrosian radii ( $R_{90}$  and  $R_{50}$ ). These are supplemented with the following parameters from the SDSS DR6 Catalog Archive Server<sup>3</sup>: velocity dispersion as measured in the SDSS 3" fiber ( $\sigma_{fib}$ ),  $r$ -band de Vaucouleurs radius ( $r_{deV}$ ) and axis ratio ( $a/b$ ), and the likelihoods of de Vaucouleurs and exponential fits to the galaxy light profiles. The non-detection of emission lines is determined using the emission line measurements of Yan et al. (2006) by requiring galaxies to have emission line fluxes below a  $2\sigma$  detection in both the  $H\alpha$  and the  $[\text{OII}]\lambda 3727$  lines. The spectra used in this analysis are downloaded from the SDSS DR6 Data Archive Server<sup>4</sup>.

The galaxy radii are critical measurements for this analysis, entering the FP determinations both directly through  $R_e$  and indirectly through the calculation of  $I_e$ . We have attempted to correct for known problems in the SDSS photometry pipeline (see Paper I) but problems may remain. To check the validity of the de Vaucouleurs  $R_e$  available in DR6, we compared these values to effective radii measured independently using the photometry package GALFIT v.2.0.3c (Peng et al. 2002), kindly provided by A. van der Wel. The GALFIT radii were measured from Sersic fits to the galaxy  $r$ -band light profile with  $n = 4$  to match the SDSS de Vaucouleurs photometry. In comparison to the GALFIT radii, the SDSS radii are slightly underestimated for the largest galaxies (low by  $\sim 0.07$  dex) and slightly overestimated for the smallest galaxies (high by  $\sim 0.1$  dex). In addition to these systematic variations, there is scatter of  $\sim 0.05$  dex between the two estimates of  $\log R_e$ . In §3.1, galaxies are sorted into bins based on  $R_e$ , with bin widths of 0.2 dex in  $\log R_e$ . Uncertainties on the order of 0.05 dex in  $\log R_e$  should therefore have only modest effects on bin assignments. To make certain that our results are not strongly affected by possible errors in the DR6 values of  $R_e$ , we have performed the entire analysis presented in this paper using both the SDSS pipeline values of  $R_e$  and the GALFIT fits to  $R_e$  and compared the differences. All the results are qualitatively identical. We have chosen

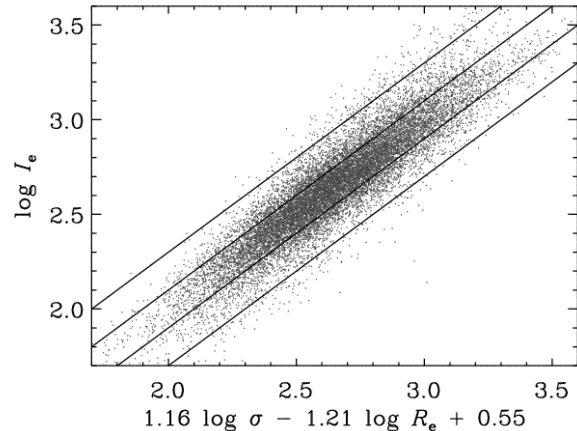


FIG. 1.— The thickness of the FP in the  $I_e$  dimension. Here, the measured value of  $\log I_e$  for each galaxy in the sample is plotted against the predicted  $\log I_e$  in terms of  $\log \sigma$  and  $\log R_e$  from the best fit to the FP. We divide the FP into “low-SB” ( $-0.3 < \Delta \log I_e < -0.1$ ), “midplane” ( $-0.1 < \Delta \log I_e < 0.1$ ), and “high-SB” ( $0.1 < \Delta \log I_e < 0.3$ ) slices based on the surface brightness residuals, as indicated by the solid lines.

to present the results based on the SDSS DR6 pipeline photometry as these values are more easily accessible to the general astronomical community.

### 3. DECONSTRUCTING THE FUNDAMENTAL PLANE

The overarching goal of this project is to understand the relation between galaxy star formation histories (SFHs) and their present-day structural properties, as categorized by their location in FP-space. To study systematic variations in SFHs with structure, galaxies are sorted into bins based on their location on the FP, then average spectra are constructed from the individual galaxies in each bin. The average spectra have very high signal-to-noise ( $S/N$ ), allowing accurate stellar population modelling of the mean SFH of galaxies at each point in FP-space. This section defines the binning and describes the stellar population modelling process.

#### 3.1. Binning in Fundamental Plane Space

In addition to studying stellar population trends over the FP, we also want to investigate variations through the thickness of the FP. We thus want to divide galaxies into bins in a three dimensional (3-D) space. There are two obvious choices for binning coordinate systems. The first is to use two orthogonal vectors within the FP, together with a third vector defined perpendicular to the FP, similar to the  $\kappa$ -space of Bender et al. (1992). The second is to use the observed structural parameters  $\log \sigma$ ,  $\log R_e$ , and  $\log I_e$  directly, despite the fact that they are not truly orthogonal. We have chosen the latter approach because the resulting trends yield more readily to interpretation.

The parameters  $\log \sigma$  and  $\log R_e$  fortunately describe a relatively face-on view of the FP. It is furthermore attractive to choose them as fundamental binning parameters because neither depends explicitly on stellar population properties (in contrast to  $I_e$ ) and because a combination of  $\sigma$  and  $R_e$  gives an estimate of the dynamical mass ( $M_{dyn}$ ) of a galaxy, thus this binning scheme groups together galaxies of similar total mass. The FP by defini-

<sup>3</sup> <http://cas.sdss.org/dr6/en>

<sup>4</sup> <http://das.sdss.org/DR6-cgi-bin/DAS>

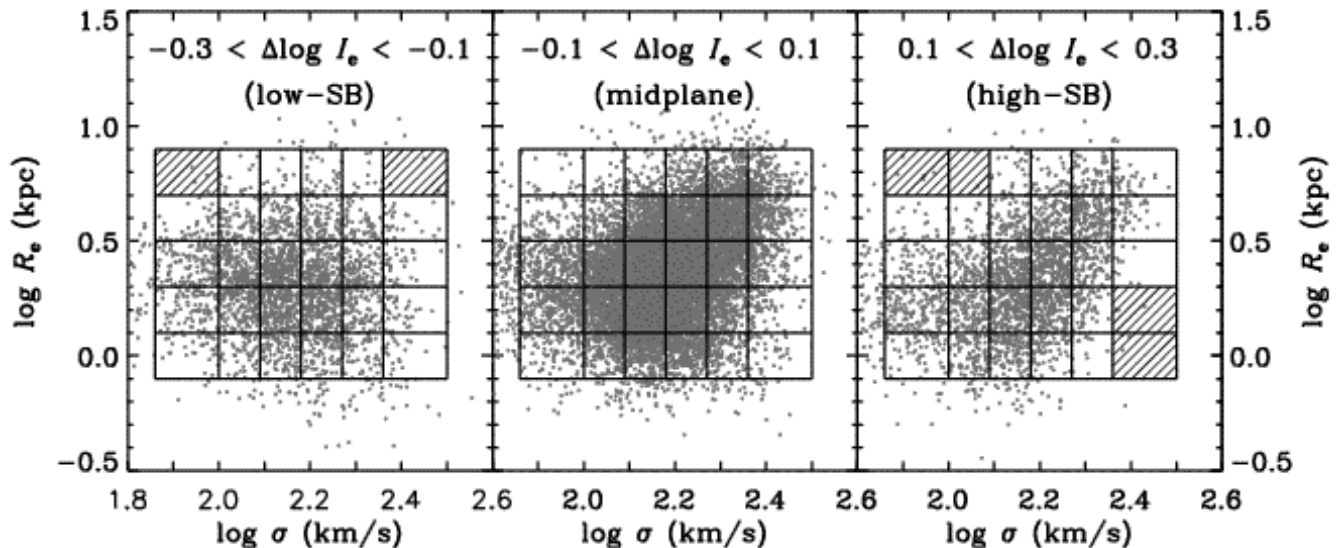


FIG. 2.— Bin definitions for the purposes of sorting and stacking galaxies across the FP. Gray points show all galaxies in the sample, while black lines indicate the bin definitions. The three panels represent the three slices in surface brightness residuals, defined in Figure 1. Galaxies are further divided into 6 bins in  $\log \sigma$  and 5 bins in  $\log R_e$  within each slice in  $\Delta \log I_e$ , as illustrated. Five of the 90 bins do not contain enough galaxies to produce robust mean spectra and are therefore excluded from our analysis. These are indicated by the shaded bins. In each of the three surface brightness slices, the galaxies occupy somewhat different parts of  $\log \sigma$ – $\log R_e$  space, indicating some curvature in the observed FP for this sample.

tion has only two independent parameters. Once  $\log \sigma$  and  $\log R_e$  have been set, the mean value of  $\log I_e$  for that bin is fixed.

We use the  $\log I_e$  dimension to explore SFH variations through the *thickness* of the FP. Treating  $\log I_e$  as the dependent variable, we fit the FP for  $\log I_e$  as a function of  $\log \sigma$  and  $\log R_e$  using a simple least squares fit that minimizes residuals in the  $\log I_e$  direction (implemented as the IDL routine *sfit.pro*) and find the relation

$$\log I_e = 1.16 \log \sigma - 1.21 \log R_e + 0.55, \quad (1)$$

where  $\sigma$ ,  $R_e$ , and  $I_e$  are in units of  $\text{km s}^{-1}$ , kpc, and  $L_\odot \text{ pc}^{-2}$ , respectively. The thickness of the FP can then be described as  $\Delta \log I_e$ , where  $\Delta$  indicates the difference between the observed value of  $\log I_e$  and the expected value of  $\log I_e$  given the observed  $\log \sigma$  and  $\log R_e$ . Figure 1 shows the observed  $\log I_e$  plotted against the best fitting FP relation given by equation 1. By defining cuts in  $\Delta \log I_e$ , the FP is sliced into three layers: “low-SB” ( $-0.3 < \Delta \log I_e < -0.1$ ), “midplane” ( $-0.1 < \Delta \log I_e < +0.1$ ), and “high-SB” ( $+0.1 < \Delta \log I_e < +0.3$ ), as shown in Figure 1. Here, the terms “low-SB” and “high-SB” are relative terms which describe the value of  $I_e$  with respect to the typical value of  $I_e$  for galaxies of the same  $\sigma$  and  $R_e$ .

More sophisticated statistical methods can be used to fit the FP relation, but the assignment of galaxies to bins is relatively insensitive to the exact equation used to describe the FP. The choice of  $\log I_e$  as the dependent parameter in the binning process is motivated by three things: the first is the previously stated fact that  $I_e$  (and not  $R_e$  or  $\sigma$ ) is expected to vary most strongly with star formation history. The second is that  $\sigma$  and  $R_e$  can be combined to estimate  $M_{\text{dyn}}$  for a galaxy, thus produc-

ing groups of galaxies of similar total mass. The third is that Paper I demonstrated that, at fixed  $\sigma$ , stellar populations vary substantially with  $\Delta \log L_V$ , which is related to  $\Delta \log I_e$ .

In each of the three surface-brightness slices, galaxies are divided by a  $6 \times 5$  grid in  $\log \sigma$  and  $\log R_e$ , as shown in Figure 2. The grid is identical for all three slices. Sorting galaxies in this 3-D space of  $\log \sigma$ – $\log R_e$ – $\Delta \log I_e$  results in 90 different bins of galaxies. Within each bin, galaxies share similar values of these three parameters, and therefore also share similar values of  $M_{\text{dyn}}$ , total luminosity ( $L_V$ ), and mass-to-light ratio ( $M_{\text{dyn}}/L$ ). Within each bin, galaxies with colors more than  $0.06 \text{ mag}^5$  from the mean  $g-r$  color of the bin are excluded so that the stellar population properties measured in each bin are not biased by a small number of interlopers. The median values of  $\log \sigma$ ,  $\log R_e$ ,  $\Delta \log I_e$ , and  $\log I_e$  for each of the 90 bins are listed in Table 1, along with the total number of galaxies in each bin.

Interestingly, Figure 2 shows that the galaxy distribution in  $\log \sigma$ – $\log R_e$  space is somewhat different in the various slices, with the high-SB slice showing a tail of high- $\sigma$ , high- $R_e$  galaxies that are not present in the low-SB slice. This occurs because the FP of our sample galaxies has a small degree of curvature. This curvature is not necessarily real and may be due to selection effects. We have not attempted to correct for selection biases in this analysis, which spans a limited range in redshift and is therefore nearly volume-limited. Because galaxies are binned by surface brightness, selection effects should result in low-SB bins being incomplete but should not substantially bias the mean spectra.

<sup>5</sup> This is the typical color spread for galaxies with the same  $\sigma$ . See section §4.1 of Paper I for details.

Of the 90 bins described here, six bins do not contain enough galaxies to produce a reliable stacked spectrum (i.e., contain 5 or fewer galaxies), leaving a total of 84 stacked spectra for the analysis. Spectra are combined using a method that rejects outlier pixels, masks bright skylines, weights all galaxies equally, and smooths all spectra to the same resolution before combining (see §4.2 of Paper I for details). The result is a high  $S/N$  mean spectrum for each bin on the FP, as well as a corresponding error spectrum.

The bins are not evenly populated. As can be seen in Figure 2 and Table 1, some of the bins contain many hundreds of galaxies, while others contain a dozen or so. The typical  $S/N$  of the individual stacked spectra therefore varies substantially between bins. It is worth bearing in mind that the error bars are not uniform for the stacked spectra. In much of the subsequent analysis, we will indicate data derived from the lower  $S/N$  spectra and present typical error bars separately for the low- $S/N$  and high- $S/N$  data.

### 3.2. Lick Indices and Stellar Population Modelling

In each of the stacked spectra, we measure the full set of Lick indices as defined in Worthey et al. (1994) and Worthey & Ottaviani (1997). These include Balmer lines  $H\beta$ ,  $H\gamma_F$ , and  $H\delta_F$  (as well as broad versions of the bluer Balmer lines,  $H\gamma_A$  and  $H\delta_A$ ), a set of Fe-dominated lines (Fe4383, Fe4531, Fe5015, Fe5270, Fe5335, Fe5406, Fe5709, and Fe5782), and lines that are also sensitive to element abundances other than Fe ( $Mg_1$ ,  $Mg_2$ ,  $Mg\ b$ ,  $CN_1$ ,  $CN_2$ ,  $C_24668$ ,  $Ca4227$ ,  $Ca4455$ ,  $NaD$ ,  $TiO_1$ , and  $TiO_2$ ). Index measurements are performed by the automated IDL code *Lick\_EW*, which is part of the publicly available<sup>6</sup> *EZ\_Ages* code package (Graves & Schiavon 2008). *Lick\_EW* also computes errors in the Lick index absorption strengths from the associated error spectra following the formalism of Cardiel et al. (1998). It should be noted that the SDSS 3'' spectral fibers sample roughly  $2/3 R_e$  for the redshift range of our sample. Index measurements and derived abundances in this work are therefore more nearly comparable to literature values measured within  $R_e$  or  $R_e/2$ , rather than central or  $R_e/8$  values. Because many early-type galaxies show strong radial metallicity gradients, central index strengths and abundances tend to be higher than those measured from a substantial fraction of the galaxy light.

All of the stacked spectra have been smoothed to match the highest- $\sigma$  galaxies in the sample ( $300\text{ km s}^{-1}$ ) in order to compare all galaxies at the same effective spectral resolution. The combined smoothing due to  $\sigma$  and the SDSS native resolution is *lower* than the resolution at which the Lick indices are defined ( $\sim 210\text{ km s}^{-1}$  at SDSS resolution); thus the linestrength measurements must be corrected to bring them onto the Lick system. We do this using corrections computed in Table A2a of Schiavon (2007). The stellar population models used to interpret the line strength measurements are based on flux calibrated spectra, and the SDSS spectra are themselves flux-calibrated; thus we do not apply a zeropoint shift to bring our index measurements fully onto the Lick system. Because the data and the models are both flux-calibrated, zeropoint offsets should be negligible.

<sup>6</sup> [http://www.ucolick.org/~graves/EZ\\_Ages.html](http://www.ucolick.org/~graves/EZ_Ages.html)

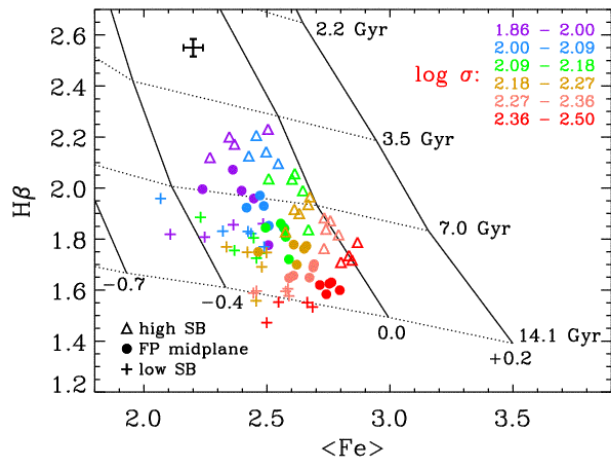


FIG. 3.— Lick index measurements for the stacked spectra, compared with a grid of stellar population models. The stellar population models shown here are computed using the average abundance pattern for the sample galaxies ( $[Mg/Fe] = +0.19$ ,  $[C/Fe] = +0.17$ ,  $[N/Fe] = +0.05$ ,  $[Ca/Fe] = +0.01$ , with  $[Na/Fe] = [Si/Fe] = [Ti/Fe] = [Mg/Fe]$ , and  $[Cr/Fe] = 0.0$ . See Graves & Schiavon 2008 for details). Solid lines connect models at constant  $[Fe/H]$ , while dotted lines connect models at constant age. A typical statistical error for the index measurements is shown in the top left. Lines of constant age (metallicity) do not run exactly horizontal (vertical) because the  $H\beta$  and  $\langle Fe \rangle$  indices are sensitive to both age and metallicity (the “age-metallicity degeneracy”). As is clear from the model grids, this degeneracy can be broken using a combination of Lick indices. The non-orthogonality of the model grids results in correlated errors in the age and  $[Fe/H]$  determinations for the stacked spectra, as discussed in §4.3.

To convert the set of line strength measurements into stellar population mean ages and abundances, the Lick indices are compared to the single stellar population models of Schiavon (2007). These models include the effects of multiple element abundance ratios and allow estimates of  $[Fe/H]$ ,  $[Mg/Fe]$ ,  $[C/Fe]$ ,  $[N/Fe]$ , and  $[Ca/Fe]$ , as well as mean luminosity-weighted stellar age. In Graves & Schiavon (2008), we created an IDL code package, *EZ\_Ages*, which automates the process of determining stellar population mean age,  $[Fe/H]$ , and abundance ratios for a set of Lick index measurements. We use *EZ\_Ages* with the “standard set” of Lick indices ( $H\beta$ ,  $\langle Fe \rangle^7$ ,  $Mg\ b$ ,  $C_24668$ ,  $CN_1$ , and  $Ca4227$ ) to determine ages,  $[Fe/H]$ , and abundance ratios for the 84 stacked spectra in our sample with adequate  $S/N$  (see §3.1)<sup>8</sup>. A detailed description of the modelling process is presented in Graves & Schiavon (2008), as well as rigorous testing of the method on Galactic globular clusters and a comparison with stellar population modelling results from Thomas et al. (2005). The interested reader is referred to that work for more information on the modelling process. It is worth noting here, however, that the models are computed at fixed  $[Fe/H]$ , rather than at fixed total metallicity ( $[Z/H]$ ) as in some stellar population models. Total metallicity is dominated by oxygen, which is unmeasurable in unresolved stellar pop-

<sup>7</sup>  $\langle Fe \rangle = \frac{1}{2} (Fe5270 + Fe5335)$

<sup>8</sup> For stacked spectrum #76, the  $H\beta$  line was weaker than any of the models. We therefore computed abundances for this spectrum using  $H\gamma_F$  instead of  $H\beta$ . Because  $H\gamma_F$  produces systematically younger age estimates than  $H\beta$  (Graves & Schiavon 2008), we have excluded this spectrum from the age analysis while retaining it for the abundance analysis.

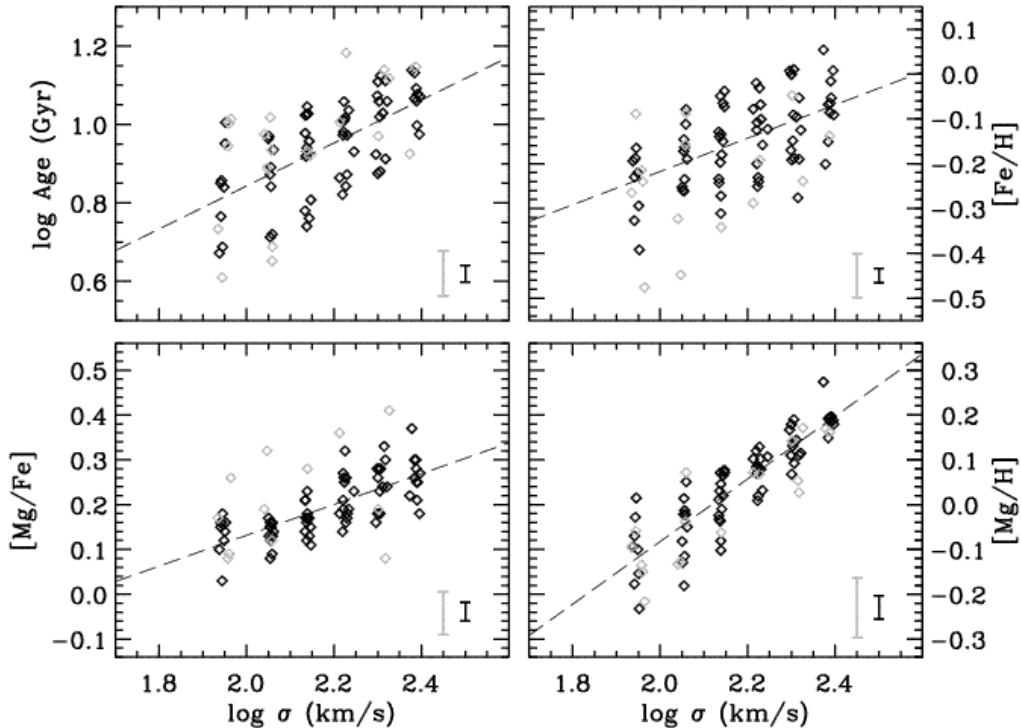


FIG. 4.— Stellar population modelling results, showing mean luminosity-weighted stellar age,  $[\text{Fe}/\text{H}]$ ,  $[\text{Mg}/\text{Fe}]$ , and  $[\text{Mg}/\text{H}]$  as a function of galaxy  $\sigma$ . Black (gray) points and error bars indicate high (low)  $S/N$  measurements and their associated median errors. Dashed lines show linear least squares fits of the stellar population properties as function of  $\sigma$ , based on the high  $S/N$  (black) data only. Mean stellar age,  $[\text{Fe}/\text{H}]$ ,  $[\text{Mg}/\text{Fe}]$ , and  $[\text{Mg}/\text{H}]$  all increase with increasing  $\sigma$ . Age and  $[\text{Fe}/\text{H}]$  both show substantial scatter at fixed  $\sigma$ , with total spread 4–5 times the expected spread due to measurements errors, indicating genuine underlying population variations at fixed  $\sigma$ .  $[\text{Mg}/\text{H}]$  and  $[\text{Mg}/\text{Fe}]$  show less scatter, only  $\sim 2$  times that expected due to measurement errors. The  $[\text{Mg}/\text{H}]$ – $\sigma$  relation is particularly strong and tight, nearly consistent with measurement errors, particularly at the high- $\sigma$  end.

ulations with current techniques. In this analysis, we specifically discuss  $[\text{Fe}/\text{H}]$  and  $[\text{Mg}/\text{H}]$ , elements which can be measured from low-resolution spectra, and avoid making statements about  $[\text{Z}/\text{H}]$ .

Figure 3 shows the measured values of  $\langle \text{Fe} \rangle$  and  $\text{H}\beta$  for the stacked spectra plotted over a set of model grids from Schiavon (2007). Data points are color-coded by  $\sigma$  as indicated in the figure key. Crosses, filled circles, and open triangles represent the low-SB, midplane, and high-SB data, respectively. The various bins in  $R_e$  are not indicated. Two trends emerge clearly from the data. As  $\sigma$  increases, galaxies tend to have *stronger*  $\langle \text{Fe} \rangle$  and *weaker*  $\text{H}\beta$ . At fixed  $\sigma$ , as  $\Delta I_e$  increases, galaxies tend to have *stronger*  $\langle \text{Fe} \rangle$  and *stronger*  $\text{H}\beta$ . We will discuss the detailed implications of these trends in §4; here they are merely presented to illustrate the linestrength data.

The solid lines in Figure 3 show models of constant  $[\text{Fe}/\text{H}]$ , from  $-0.7$  to  $+0.2$ , as labelled. The dotted lines show models of constant age, from 2.2 to 14.1 Gyr. As can be seen from the orientation of the grid lines,  $\text{H}\beta$  is predominantly sensitive to stellar population age such that younger populations have stronger  $\text{H}\beta$ , while  $\langle \text{Fe} \rangle$  is dominated by  $[\text{Fe}/\text{H}]$  such that more Fe-rich populations have stronger  $\langle \text{Fe} \rangle$ . The effects of the age-metallicity degeneracy are apparent in the fact that  $\text{H}\beta$  is (mildly) sensitive to  $[\text{Fe}/\text{H}]$  and  $\langle \text{Fe} \rangle$  is sensitive to age. Because of the degeneracy, there is no one-to-one mapping between  $\text{H}\beta$  and age, or  $\langle \text{Fe} \rangle$  and  $[\text{Fe}/\text{H}]$ ; the grid lines are not per-

fectly vertical and horizontal. However, the model grids in these particular indices are close enough to orthogonal that they serve to break the age-metallicity degeneracy. Other combinations of indices (e.g.,  $\text{H}\delta_F$  and  $\text{Fe}4383$ , see Figure 9 of Graves & Schiavon 2008) are more affected by the degeneracy, causing the model grids to collapse down on top of one another and making them less robust indicators of age and metallicity.

*EZ\_Ages* computes statistical errors in each of the stellar population parameters, determined from the measurement errors in the Lick indices. The black cross in the upper left corner of Figure 3 illustrates the median errorbars in the line strength measurements. The non-orthogonality of the model grids due to the age-metallicity degeneracy causes the derived errors to be correlated. For example, an overestimate of  $\langle \text{Fe} \rangle$  will result in both a higher derived value of  $[\text{Fe}/\text{H}]$  and a slightly lower derived value for the age. The age-metallicity degeneracy therefore causes correlated errors in the stellar population parameters, which must be taken into account when interpreting results. In general, however, the very high  $S/N$  of the stacked spectra in this analysis make the stellar population modelling results robust to such effects. The effect of correlated errors will be discussed in greater detail in §4.3.

This paper discusses only the mean luminosity-weighted ages,  $[\text{Fe}/\text{H}]$ , the abundance ratio  $[\text{Mg}/\text{Fe}]$ , and  $[\text{Mg}/\text{H}]$  (which is simply  $[\text{Mg}/\text{Fe}] + [\text{Fe}/\text{H}]$ ). The re-

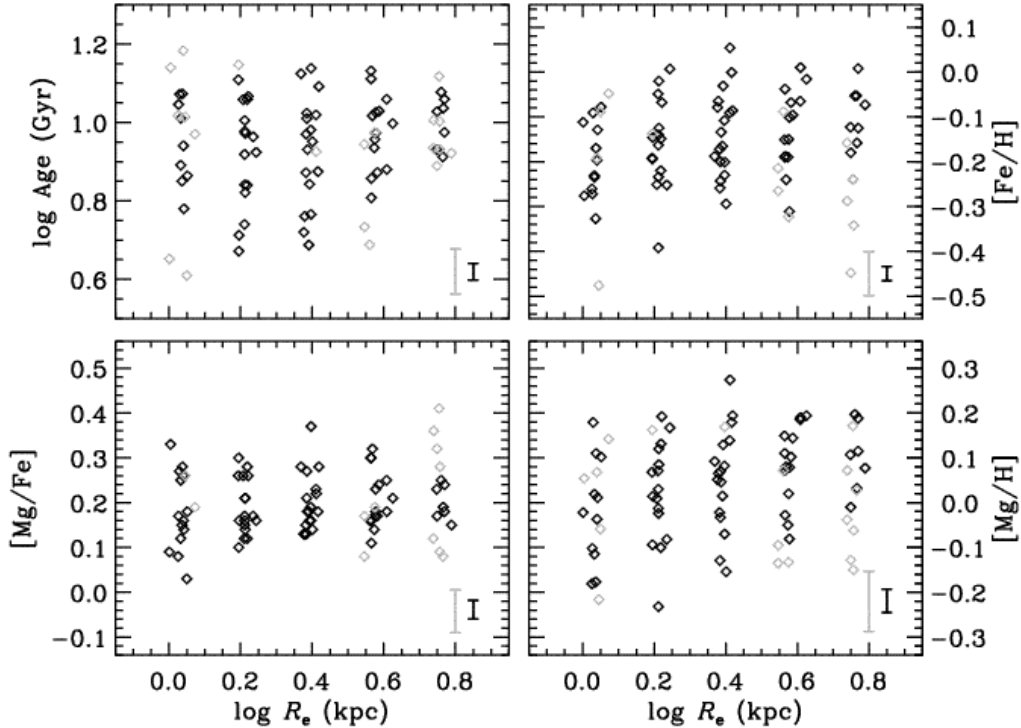


FIG. 5.— Stellar population modelling results, showing mean luminosity-weighted stellar age,  $[\text{Fe}/\text{H}]$ ,  $[\text{Mg}/\text{Fe}]$ , and  $[\text{Mg}/\text{H}]$  as a function of galaxy  $R_e$ . Black (gray) points and error bars indicate high (low)  $S/N$  measurements and their associated median errors. No strong correlations are observed between  $R_e$  and any stellar population properties, implying that galaxy star formation histories are nearly independent of galaxy size.

sults of the stellar population fits are given in Table 2, along with the Lick indices from which these parameters are determined. Discussion of other abundance ratios is deferred to future work. An important caveat about the stellar population parameters discussed here is that they represent mean, luminosity-weighted averages over all the stars in a galaxy, which additionally have been averaged over all galaxies which contribute to a stacked spectrum. A younger mean age measured in one stacked spectrum compared to another does not make a definitive statement about the ages of all stars in all galaxies in that bin: it could also mean that all of the galaxies in that bin contain sub-populations of younger stars, or that some of the galaxies in the bin have generally younger stars. There is also a strong degeneracy between the age of a younger subpopulation and the mass fraction it comprises: mean ages can be skewed younger by a small population of very young stars, or by a larger population of somewhat less young stars. Age measurements should therefore be treated as a statistical description of galaxies in the bin, rather than as “true” ages for all the stars in an individual galaxy.

#### 4. STELLAR POPULATIONS IN FUNDAMENTAL PLANE SPACE

##### 4.1. Age, $[\text{Fe}/\text{H}]$ , $[\text{Mg}/\text{H}]$ , and $[\text{Mg}/\text{Fe}]$ as Functions of $\sigma$ , $R_e$ , and $I_e$ Separately

We begin by examining the variations in stellar population properties with each of the FP parameters  $\sigma$ ,  $R_e$ , and  $I_e$  individually.

Figure 4 shows the *EZ\_Ages* results for mean luminosity-weighted age,  $[\text{Fe}/\text{H}]$ ,  $[\text{Mg}/\text{H}]$ , and  $[\text{Mg}/\text{Fe}]$  as a function of the median  $\log \sigma$  in each galaxy bin. We have divided the data into “low- $S/N$ ” and “high- $S/N$ ” subsamples in order to indicate the range of error values, where low- $S/N$  data points are those whose statistical error estimates are  $> 0.015$  dex higher than the median error value for the data as a whole. The black data points and error bars indicate the values associated with high- $S/N$  data. Low- $S/N$  data are indicated in gray, along with the appropriate median error bar. Age, total Fe and Mg abundances, and the  $[\text{Mg}/\text{Fe}]$  abundance ratio all increase with increasing  $\sigma$ . These relations are very similar to those demonstrated in Paper I, where galaxies were binned first by  $\sigma$  and then by  $L$  and color at fixed  $\sigma$ . Dashed lines indicated linear least squares fits of the stellar population parameters as functions of  $\sigma$ , computed using only the high  $S/N$  data (i.e., excluding the gray points).

The age- $\sigma$  and  $[\text{Fe}/\text{H}]$ - $\sigma$  relations both show substantial scatter. Quantitatively, the spread around the mean relations (dashed lines) is  $\sim 4$ – $5$  times larger than the scatter expected due to the statistical errors in both age and  $[\text{Fe}/\text{H}]$ , indicating that there is substantial spread in the star formation histories of galaxies at fixed  $\sigma$ . The  $[\text{Mg}/\text{Fe}]$ - $\sigma$  and  $[\text{Mg}/\text{H}]$ - $\sigma$  relations show less scatter, with the observed spread representing only  $\sim 2$  times the expected statistical scatter. The Mg abundance shows both the steepest correlation with  $\sigma$  and the least intrinsic scatter about the mean relation as compared to the



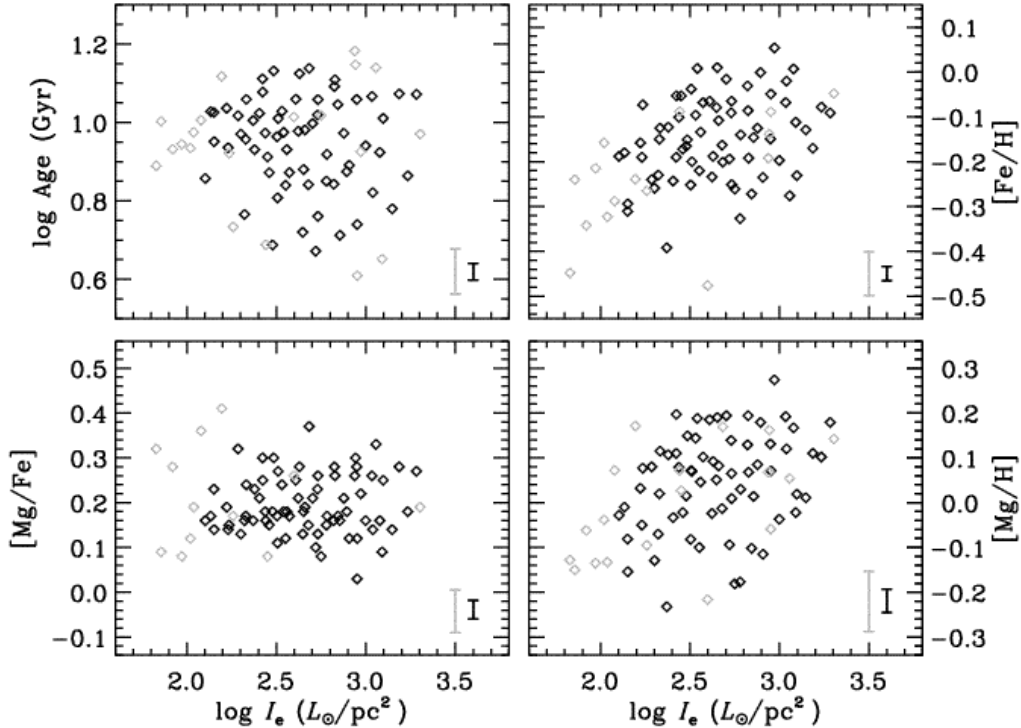


FIG. 6.— Stellar population modelling results, showing mean luminosity-weighted stellar age,  $[\text{Fe}/\text{H}]$ ,  $[\text{Mg}/\text{Fe}]$ , and  $[\text{Mg}/\text{H}]$  as a function of galaxy  $I_e$ . Black (gray) points and error bars indicate high (low)  $S/N$  measurements and their associated median errors. Weak trends are visible, such that stellar population age decreases slightly with increasing  $I_e$ , while  $[\text{Fe}/\text{H}]$  and  $[\text{Mg}/\text{H}]$  increase slightly with increasing  $I_e$ , but none of these trends are compelling.  $[\text{Mg}/\text{Fe}]$  appears entirely independent of  $I_e$ .

observational errors, indicating that  $[\text{Mg}/\text{H}]$  varies only slightly at fixed  $\sigma$ .

Unlike the strong stellar population trends observed with  $\sigma$ , neither  $R_e$  nor  $I_e$  shows strong correlations with stellar population properties. Figure 5 shows the results of the stellar population modelling as a function of the median  $\log R_e$  for each galaxy bin. There are no strong trends with  $R_e$  in any of the properties modelled here. There is some evidence for slight increases in  $[\text{Fe}/\text{H}]$  and  $[\text{Mg}/\text{H}]$  with increasing  $R_e$ , but the dependence is weak and the scatter is large. Also, at large  $R_e$  there do not appear to be any “young” galaxies with mean ages  $< 7$  Gyr. However, it is evident from Figure 2 that there are very few galaxies with large  $R_e$  and low  $\sigma$ . Since Figure 4 showed that low- $\sigma$  galaxies are most likely to have young ages, the lack of “young” galaxies with large  $R_e$  may be due to the way galaxies populate the FP, rather than any genuine relation between larger  $R_e$  and older ages.

Finally, Figure 6 shows age,  $[\text{Fe}/\text{H}]$ ,  $[\text{Mg}/\text{Fe}]$ , and  $[\text{Mg}/\text{H}]$  plotted against the median  $\log I_e$  for each galaxy bin. Again, there are no strong correlations between  $\log I_e$  and any of the stellar population parameters. There is some indication of weak correlations between  $\log I_e$  and  $[\text{Fe}/\text{H}]$  and  $[\text{Mg}/\text{H}]$  such that the high-SB galaxies have higher Fe and Mg abundances. There is also some evidence for a weak anti-correlation between  $\log I_e$  and age such that low-SB galaxies have older ages, but none of these trends is compelling. The  $[\text{Mg}/\text{Fe}]$  abundance ratio is completely flat with  $\log I_e$ .

A clear result from Figures 4–6 is that stellar popula-

tions on the FP vary primarily with  $\sigma$ . Neither  $R_e$  nor  $I_e$  appears to be closely related to stellar population properties. However, the lack of general trends with  $R_e$  and  $I_e$  may hide weak correlations with residuals from the strong  $\sigma$  relationships. Although Figure 4 shows clear correlations with  $\sigma$  in all stellar population parameters, there is some scatter at fixed  $\sigma$ , particularly in age and  $[\text{Fe}/\text{H}]$ . The next section examines how stellar populations vary throughout the FP as a function of all three FP parameters simultaneously.

#### 4.2. Mapping Stellar Populations Along and Through the Fundamental Plane

By binning galaxies along and through the thickness of the FP, then stacking their spectra and performing stellar population modelling on the high  $S/N$  average spectra, we have measured the typical age,  $[\text{Fe}/\text{H}]$ ,  $[\text{Mg}/\text{H}]$ , and  $[\text{Mg}/\text{Fe}]$  for galaxies at each point on, above, and below the FP. Each of these properties can be mapped throughout the 3-D space of the FP, thereby associating information about typical star formation histories with the structural properties of galaxies. This is a somewhat challenging exercise in data visualization, as we are trying to understand the variations and co-variations of four different stellar population parameters throughout a 3-D structure space. This effectively involves probing a 7-D parameter space, although by focusing on one stellar population parameter at a time, we can limit it to a 4-D space. In this and the next section, we attempt to codify trends in this 7-D space and understand how the various



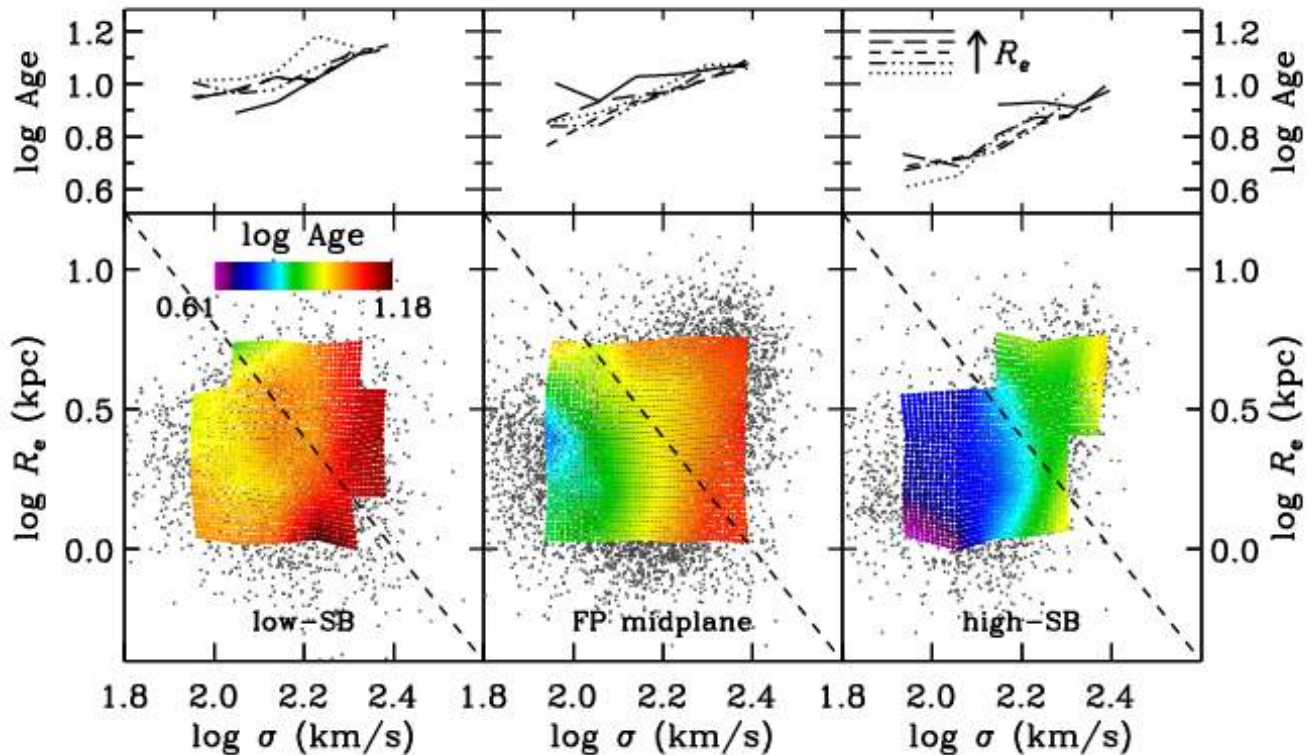


FIG. 7.— Mean luminosity-weighted stellar population age, mapped across the FP. The three lower panels show the three slices in surface brightness, as in Figure 2. Within each slice, galaxy  $\sigma$  and  $R_e$  are plotted, with gray points showing individual galaxies in the sample. The overplotted color contours show the typical stellar population age at each point on the FP (see §4.2 for details). The dashed lines show lines of constant  $M_{dyn}$ , assuming  $M_{dyn} \propto \sigma^2 R_e$ . Within each slice, age increases with increasing  $\sigma$ , as seen in Figure 5. Lines of constant age run approximately vertically, indicating that mean stellar population age is independent of  $R_e$  at fixed  $\sigma$ . The upper panels show stellar population age as a function of  $\sigma$  for each FP slice. Different values of  $R_e$  are indicated by different line styles. Comparing the typical ages between the various slices in  $I_e$ , it is clear that galaxies with lower surface brightness than the FP (left panels) have *older* ages than those on the FP midplane (center panels), while galaxies with higher surface brightness than the FP (right panels) have *younger* ages, at the same value of  $\sigma$  and  $R_e$ . Despite the lack of strong stellar population trends with absolute galaxy  $I_e$  (c.f., Figure 6), stellar population age at fixed  $\sigma$  does appear to depend on  $I_e$  residuals from the FP, such that low-SB (high-SB) galaxies are older (younger) than those on the FP midplane.

galaxy properties correlate with one another. We begin by mapping each of the four stellar population properties along and through the FP.

Figure 7 shows the results for mean luminosity-weighted age. The figure is constructed to be similar to Figure 2, which illustrated the bin definitions for the 3-D FP space. The three lower panels show the three slices in  $\Delta \log I_e$ , with the center panel showing the midplane slice through the FP, while the left and right panels show respectively the low-SB and high-SB slices from Figure 1. Within each FP slice,  $\log \sigma$  and  $\log R_e$  are plotted for the individual galaxies as gray points (as in Figure 2). Dashed lines show lines of constant  $M_{dyn}$ . The color overlay indicates the mean stellar population age at each point in the parameter space, with numerical values given by the color bar in the top of the leftmost panel. The age overlay was constructed as follows: for each stacked spectrum, the median values of  $\log \sigma$  and  $\log R_e$  are plotted for the galaxies in the bin, color-coded by the age measured in the stacked spectrum. Ages are then interpolated between the median points to create a continuous map of stellar population age across the  $\log \sigma$ – $\log R_e$  diagram. High- $S/N$  and low- $S/N$  data are all included in the interpolation.

The upper three panels of Figure 7 show mean luminosity-weighted age as a function of  $\sigma$  for each FP slice. Different bins in  $R_e$  are indicated by different line styles.

Look first at the central panels of Figure 7, which show the midplane of the FP. The trend from Figure 4 is visible: galaxies with larger  $\sigma$  are older (red) than galaxies with lower  $\sigma$  (blue). Although there are significant changes in age as a function of  $\sigma$ , there seems to be little if any variation in age as a function of  $R_e$ . Lines of constant age run roughly vertically in the diagram. This is consistent with Figure 5, which showed no clear systematic variation in stellar population age as a function of  $R_e$ , independently of the other FP parameters. Here we see directly that, at fixed  $\sigma$ , there is no substantial dependence of stellar population age on  $R_e$ . If the best predictor of stellar population age were  $M_{dyn}$  rather than  $\sigma$ , lines of constant age should follow the dashed line of constant  $M_{dyn}$ . The near-verticality of the age contours indicates that  $\sigma$  is a better predictor of stellar population age than is  $M_{dyn}$ .

If we look now at the galaxies from the low-SB (left panels) and high-SB (right panels) slices above and below the FP, we see essentially the same trends: age increases

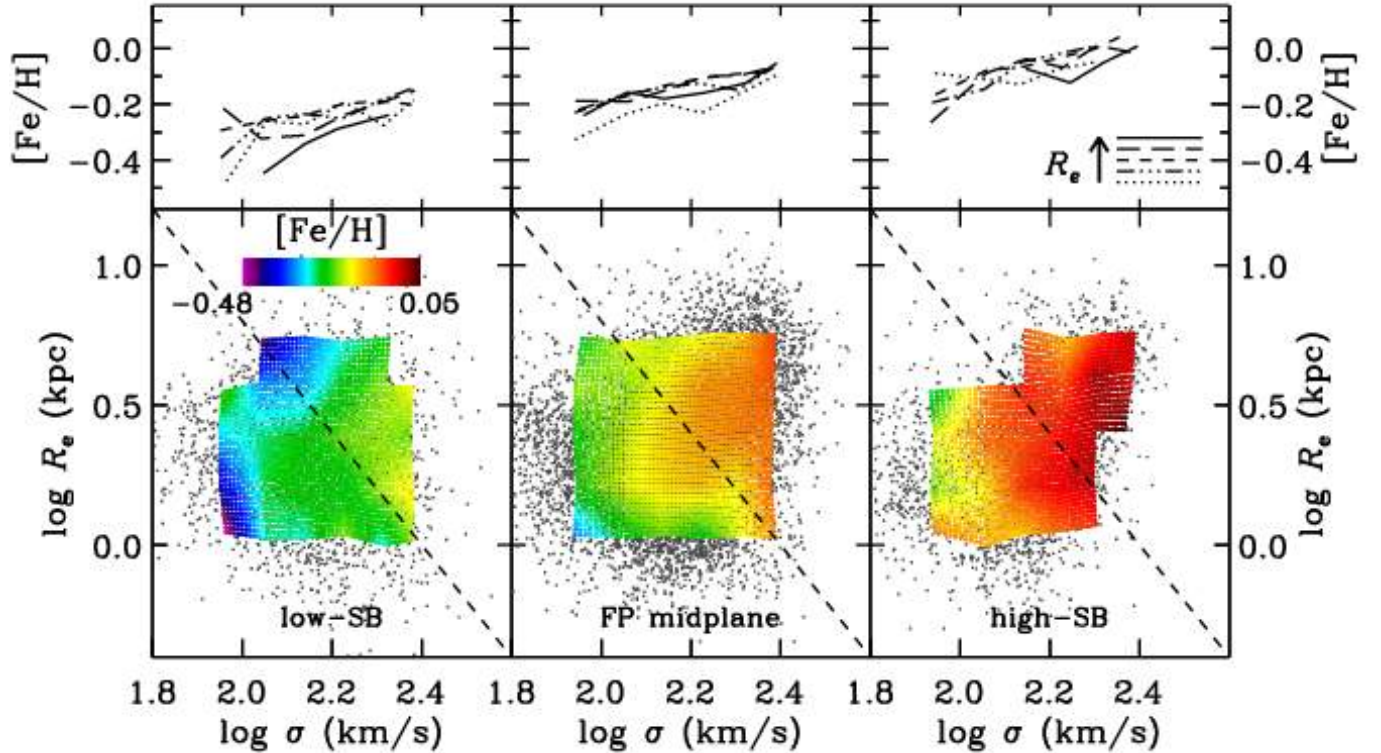


FIG. 8.— Mean stellar population  $[\text{Fe}/\text{H}]$ , mapped across the FP. The three lower panels show the three slices in surface brightness, as in Figure 2. Within each slice, galaxy  $\sigma$  and  $R_e$  are plotted, with gray points showing individual galaxies in the sample. The overplotted color contours show the typical  $[\text{Fe}/\text{H}]$  at each point on the FP. The dashed lines show lines of constant  $M_{\text{dyn}}$ , assuming  $M_{\text{dyn}} \propto \sigma^2 R_e$ . Within each slice,  $[\text{Fe}/\text{H}]$  increases with increasing  $\sigma$ , as in Figure 4.  $[\text{Fe}/\text{H}]$  appears to be relatively independent of  $R_e$ , with contours of equal  $[\text{Fe}/\text{H}]$  running nearly vertically in all slices. The upper panels show  $[\text{Fe}/\text{H}]$  as a function of  $\sigma$  for each FP slice. Different values of  $R_e$  are indicated by different line styles. Comparing the various slices in surface brightness, low-SB galaxies (left panels) appear to have lower  $[\text{Fe}/\text{H}]$  than galaxies on the midplane of the FP (center panels) at the same  $\sigma$  and  $R_e$ , while high-SB galaxies (right panels) have higher  $[\text{Fe}/\text{H}]$ . Combining these results with those apparent in Figure 7 suggests that, at fixed  $\sigma$ , stellar population age and  $[\text{Fe}/\text{H}]$  are *anti-correlated*.

systematically with increasing  $\sigma$ , but lines of constant age run nearly vertically, indicating that stellar population age is independent of  $R_e$  at fixed  $\sigma$ . However, comparing the age *ranges* (indicated by the color scale) between the different panels, there are systematic differences. These are illustrated clearly in the upper panels. Galaxies in the low-SB slice of the FP (left panels) are systematically older than galaxies in the midplane of the FP (center panels), which are in turn systematically older than galaxies in the high-SB slice (right panels). There are substantial overlaps in the age ranges in the three panels, but *at fixed*  $\sigma$  the low-SB galaxies are older and the high-SB galaxies are younger than the typical galaxies in the FP. This means that, although there are no clear trends in stellar population age with  $I_e$  alone (Figure 6), typical galaxy ages do vary with  $\Delta \log I_e$  at a fixed point in  $\sigma$  and  $R_e$ . This is similar to the results of Forbes et al. (1998) and Terlevich & Forbes (2002), who found that surface brightness residuals from the FP correlate with stellar population age, although they explored only the general trend over all galaxies, not as a function of  $\sigma$  and  $R_e$ . Our higher-resolution map is made possible through the large sample of 16,000 galaxies in this study.

A similar map for  $[\text{Fe}/\text{H}]$  is shown in Figure 8. As seen in Figure 4,  $[\text{Fe}/\text{H}]$  increases systematically with  $\sigma$ . Like stellar population age,  $[\text{Fe}/\text{H}]$  appears to de-

pend weakly or negligibly on  $R_e$ —contours of constant  $[\text{Fe}/\text{H}]$  are roughly vertical rather than following the lines of constant  $M_{\text{dyn}}$ . Also similar to the age variations, there appear to be systematic variations in  $[\text{Fe}/\text{H}]$  between the different slices in  $\Delta \log I_e$ . This trend, however, runs opposite to the one seen in age: at fixed  $\sigma$ , the low-SB galaxies (left panels) tend to be Fe-poor and the high-SB galaxies (right panels) tend to be Fe-rich. The general conclusion is that, not only do age and  $[\text{Fe}/\text{H}]$  increase with  $\sigma$ , they also vary systematically with  $\Delta \log I_e$ , with low-SB galaxies showing older mean ages and lower  $[\text{Fe}/\text{H}]$ , while high-SB galaxies show younger mean ages and higher  $[\text{Fe}/\text{H}]$ . This implies that, at fixed  $\sigma$ , age and  $[\text{Fe}/\text{H}]$  are *anti-correlated*, as first shown by Trager et al. (2000). Section 4.3 will directly examine the correlations between various stellar population residuals from the mean trends with  $\sigma$ .

Figure 9 shows the map for  $[\text{Mg}/\text{H}]$ . As expected from Figure 4,  $[\text{Mg}/\text{H}]$  varies strongly with  $\sigma$ . Like stellar population age and  $[\text{Fe}/\text{H}]$ ,  $[\text{Mg}/\text{H}]$  shows no dependence on  $R_e$ . Unlike age and  $[\text{Fe}/\text{H}]$ ,  $[\text{Mg}/\text{H}]$  varies only mildly with  $\Delta \log I_e$ . To the extent that  $[\text{Mg}/\text{H}]$  does vary at fixed  $\sigma$  between the different panels, it follows the same trend as  $[\text{Fe}/\text{H}]$ , with low-SB galaxies showing slightly lower  $[\text{Mg}/\text{H}]$  and high-SB galaxies showing slightly higher  $[\text{Mg}/\text{H}]$  than their counterparts in the

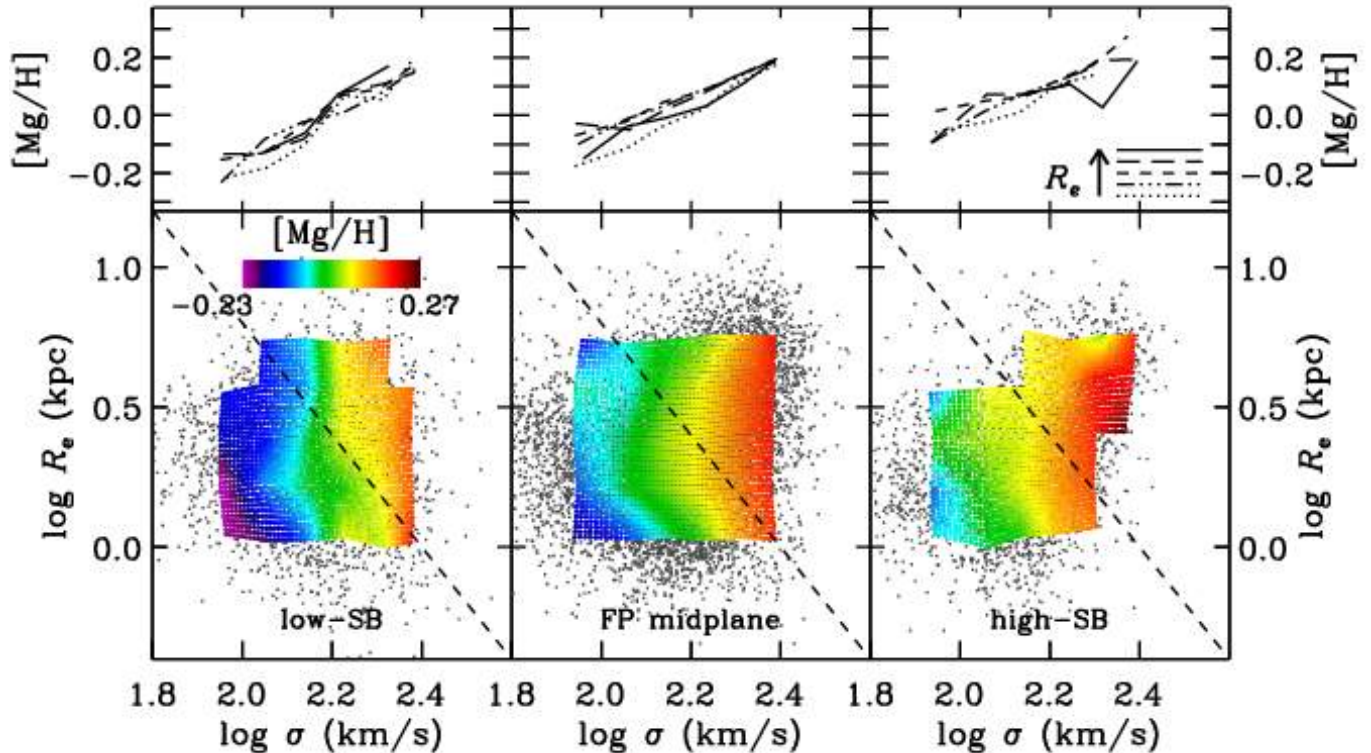


FIG. 9.— Mean stellar population  $[Mg/H]$ , mapped across the FP. The three lower panels show the three slices in surface brightness, as in Figure 2. Within each slice, galaxy  $\sigma$  and  $R_e$  are plotted, with gray points showing individual galaxies in the sample. The overplotted color contours show the typical  $[Mg/H]$  at each point on the FP. The dashed lines show lines of constant  $M_{dyn}$ , assuming  $M_{dyn} \propto \sigma^2 R_e$ . Within each slice,  $[Mg/H]$  increases strongly with increasing  $\sigma$ , as in Figure 4. Like age and  $[Fe/H]$ ,  $[Mg/H]$  appears to be relatively independent of  $R_e$ , with contours of equal  $[Mg/H]$  running nearly vertically in all slices. The upper panels show  $[Mg/H]$  as a function of  $\sigma$  for each FP slice. Different values of  $R_e$  are indicated by different line styles. Comparing the various slices of the FP, there appears to be little variation in  $[Mg/H]$  between the low-SB galaxies (left panels), the FP midplane galaxies (center panels), and the high-SB galaxies (right panels) at fixed  $\sigma$  and  $R_e$ . There is a slight tendency for high-SB galaxies to have higher  $[Mg/H]$ , but the trend with  $\Delta \log I_e$  is substantially weaker than that observed for  $[Fe/H]$  in Figure 8.

midplane FP slice. However, the variation in  $[Mg/H]$  with  $\Delta \log I_e$  is only about half that seen in  $[Fe/H]$ . Figure 4 showed that  $[Mg/H]$  has the strongest and tightest trend with  $\sigma$ . This 4-D map both confirms that there is little spread in  $[Mg/H]$  at fixed  $\sigma$  and illustrates that the small existing spread is correlated with  $\Delta \log I_e$ .

Finally, Figure 10 shows the map of  $[Mg/Fe]$  across the FP slices. As with the other stellar population parameters,  $[Mg/Fe]$  depends strongly on  $\sigma$  and is independent of  $R_e$ . Comparison between the panels shows that it also varies with  $\Delta \log I_e$ . Unlike  $[Fe/H]$  and  $[Mg/H]$ , both of which *increase* with increasing surface brightness,  $[Mg/Fe]$  *decreases* on average in high-SB galaxies (right panels) and *increases* on average in low-SB galaxies (left panels). In this respect,  $[Mg/Fe]$  behaves similarly to stellar population age, showing the highest values in low-SB, older galaxies.

It is interesting that the low-SB slice of the FP (left panels) shows substantially more total variation in  $[Mg/Fe]$  than do the other panels. This trend is consistent through all three slices. Indeed, the high- $I_e$  slice (right panels) shows only a small range of  $[Mg/Fe]$ , while the low- $I_e$  slice (left panels) shows substantial variation. An equally valid way to state this (although perhaps harder to see clearly in Figure 10) would be to say that high- $\sigma$  galaxies (at the right side of each map) show sub-

stantial variation in  $[Mg/Fe]$  between galaxies, but that the low- $\sigma$  galaxies (at the left side of each map) all have similarly low values of  $[Mg/Fe]$ .

Taken together, these maps of stellar population parameters along and through the FP show that age,  $[Fe/H]$ ,  $[Mg/H]$ , and  $[Mg/Fe]$  all vary strongly with  $\sigma$ , but that they also appear to vary with  $\Delta \log I_e$  ( $[Mg/H]$  varies only mildly, while the other three parameters vary substantially). None of them varies significantly with  $R_e$ . From these maps, it is clear that the spread around the  $\sigma$  relations shown in Figure 4 is not just due to statistical errors but in fact is systematic behavior that is correlated with surface brightness differences. This furthermore implies that there are substantial correlations between stellar population properties at fixed  $\sigma$ . The next section looks explicitly at the correlations between residuals from the  $\sigma$ -driven relations of Figure 4 in order to understand the systematic co-variation of the various stellar population properties.

#### 4.3. Residuals from the Stellar Population- $\sigma$ Relations

Stellar population residuals  $\Delta(\log \text{age})$ ,  $\Delta[Fe/H]$ ,  $\Delta[Mg/H]$ , and  $\Delta[Mg/Fe]$  are defined with respect to the mean relations versus  $\sigma$  by subtracting the linear fits shown in Figure 4 (dashed lines). Figure 11 shows various correlations between these residuals. Filled circles



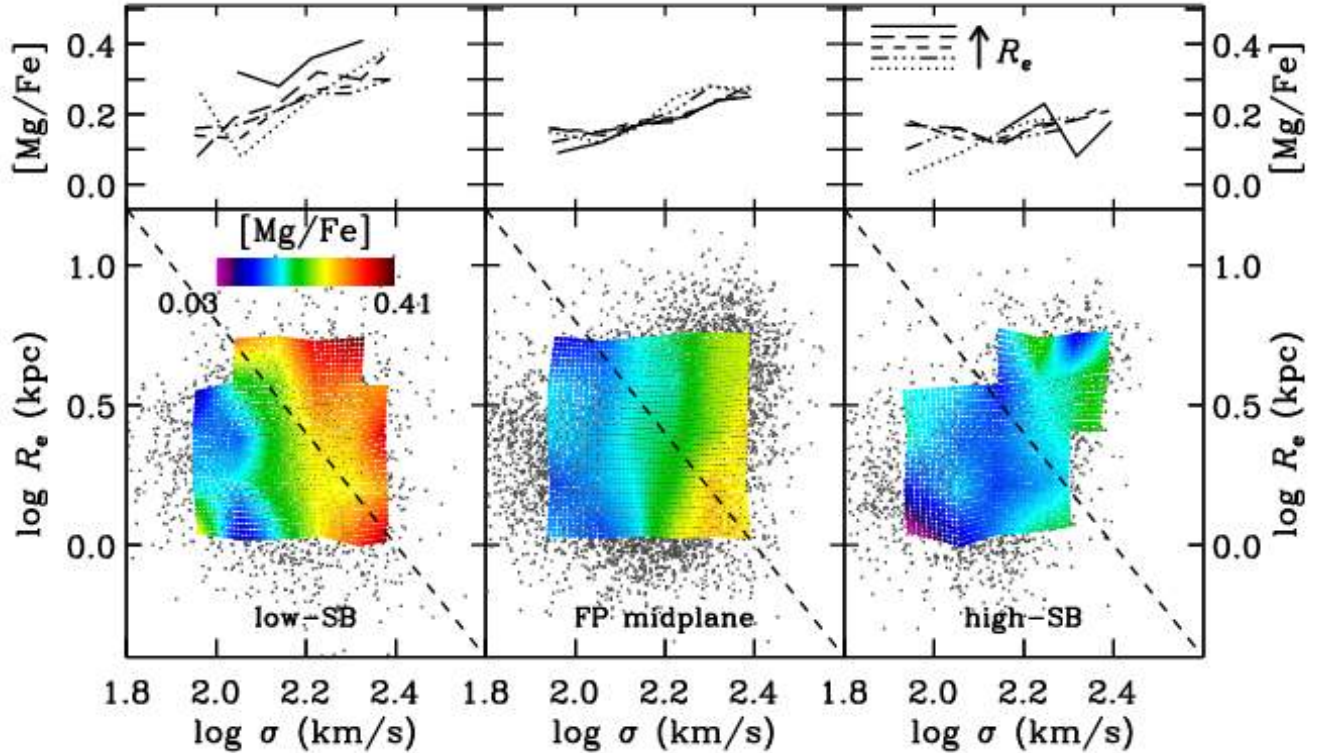


FIG. 10.— Mean stellar population  $[\text{Mg}/\text{Fe}]$ , mapped across the FP. The three lower panels show the three slices in surface brightness, as in Figure 2. Within each slice, galaxy  $\sigma$  and  $R_e$  are plotted, with gray points showing individual galaxies in the sample. The overplotted color contours show the typical  $[\text{Mg}/\text{Fe}]$  at each point on the FP. The dashed lines show lines of constant  $M_{\text{dyn}}$ , assuming  $M_{\text{dyn}} \propto \sigma^2 R_e$ . Within each slice,  $[\text{Mg}/\text{Fe}]$  increases strongly with increasing  $\sigma$ , as in Figure 4. Like the other stellar population parameters,  $[\text{Mg}/\text{Fe}]$  appears to be relatively independent of  $R_e$ , with contours of equal  $[\text{Mg}/\text{Fe}]$  running nearly vertically in all slices. The upper panels show  $[\text{Mg}/\text{Fe}]$  as a function of  $\sigma$  for each FP slice. Different values of  $R_e$  are indicated by different line styles. On average, low-SB galaxies (left panels) have higher  $[\text{Mg}/\text{Fe}]$  than those on the FP midplane (center panels), which in turn have higher  $[\text{Mg}/\text{Fe}]$  than the high-SB galaxies (right panels). The low-SB galaxies show a strong increase in  $[\text{Mg}/\text{Fe}]$  with  $\sigma$ , while the high-SB galaxies show very little overall variation in  $[\text{Mg}/\text{Fe}]$ . Another way to state this trend is that, at low  $\sigma$  (leftmost galaxies in each panel), all galaxies have relatively low values of  $[\text{Mg}/\text{Fe}]$ , while at high  $\sigma$  (rightmost galaxies in each panel), there is a substantial range in  $[\text{Mg}/\text{Fe}]$ .

show the high- $S/N$  data (corresponding to black points in Figure 4), while empty circles show the low- $S/N$  data (gray points in Figure 4). Data points are color-coded by  $\Delta \log I_e$ , with blue representing the high-SB slice of the FP, green representing the midplane of the FP, and red showing the low-SB slice of the FP.

As discussed in §3.2, the age-metallicity degeneracy results in correlated errors in the stellar population modelling process. Correlated errors arise because all absorption indices are sensitive to both age and metallicity, resulting in model grid lines that are not orthogonal in index-index space (see Figure 3). The error ellipses in the lower left corners of Figure 11 indicate the slope of the correlated errors from the stellar population modelling, as determined by Monte Carlo simulations in Graves & Schiavon (2008, see Figure 3 of that work). The solid black and dashed gray error ellipses correspond to the median errors for high- and low- $S/N$  data, respectively, based on the error estimates for the stellar population parameters determined by *EZ\_Ages*.

From Figure 11, it is clear that there are significant correlations between the residuals from the mean relations with  $\sigma$ . These correlations are strongly associated with  $\Delta \log I_e$  and thus represent real variations in star formation histories for galaxies with the same  $\sigma$ . Al-

though the correlated residuals in panels a–c are in the same direction as the correlated errors from the stellar population modelling process, the residuals trends cannot be explained merely by the correlated errors, for two reasons. In all cases, the black error ellipses are far too small to account for the observed spread in residuals, so the degeneracies in the modelling process cannot produce the observed spread in the data. Even more conclusively, the residuals depend strongly on  $\Delta \log I_e$ . This cannot be explained by measurement errors in the absorption line strengths propagated through the correlated errors in the stellar population modelling because the sense of the measurement errors should be random, not dependent on  $\Delta \log I_e$ . Thus the known degeneracies of the modelling process *cannot* account for the observed correlation of residuals. The appendix further demonstrates that correlated systematic errors due to multi-burst stellar population models also cannot be responsible for the observed trends.

Figure 11a indicates that there is a strong *anti*-correlation between stellar population age and  $[\text{Fe}/\text{H}]$  at fixed  $\sigma$ , such that high-SB galaxies tend to be younger and more Fe-rich than their low-SB counterparts at the same  $\sigma$ . The total spread is at least a factor of two (0.3 dex) in both age and Fe abundance, with  $\Delta[\text{Fe}/\text{H}]$

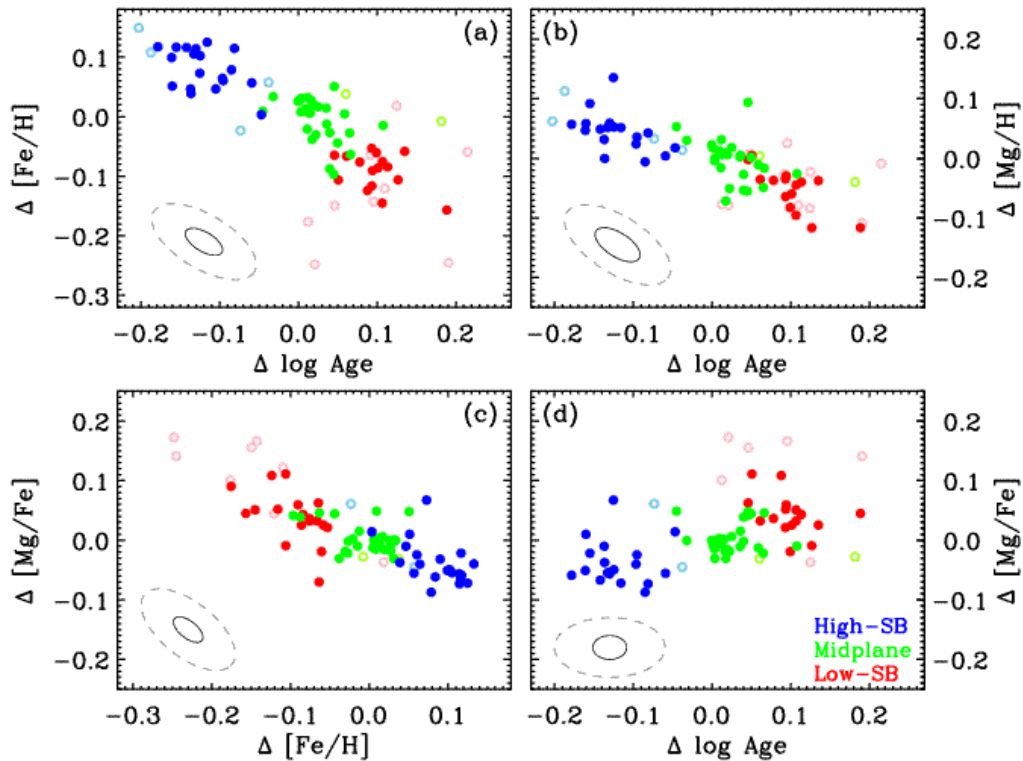


FIG. 11.— Residuals from the mean stellar population trends with  $\sigma$ , color-coded by surface brightness residuals from the FP ( $\Delta \log I_e$ ). The  $\Delta$  value for each stellar population parameter is determined by subtracting from the measured value the mean relation given by the dashed line in Figure 4. In each panel, solid (open) circles and black (gray)  $1-\sigma$  error ellipses represent high (low)  $S/N$  data and the corresponding measurement errors. Error ellipses show the direction of the correlated errors in the age and abundance determinations. Data are color-coded by galaxy surface brightness, with galaxies in the low-SB, midplane, and high-SB FP slices shown in red, green, and blue, respectively. Stellar population residuals from the trends with  $\sigma$  are clearly correlated with one another and with  $\Delta \log I_e$  such that, at fixed  $\sigma$ , low-SB galaxies tend to be older, Fe-poor, Mg-poor, and enhanced in  $[\text{Mg}/\text{Fe}]$  compared to galaxies in the FP midplane, while high-SB galaxies are younger, Fe-rich, Mg-rich, and with lower  $[\text{Mg}/\text{Fe}]$ .

$\propto -0.7\Delta(\log \text{age})$ . A similar anti-correlation was noted by Trager et al. (2000) and more recently by Smith et al. (2008b), whose error estimates for individual galaxies were small enough to allow them to claim a genuine anti-correlation in the parameters. The clear dependence of age and  $[\text{Fe}/\text{H}]$  residuals on  $\Delta \log I_e$  shown in Figure 11a lays to rest any doubts that the anti-correlation could be due to errors alone, even though the slope of the anti-correlation is similar to the expected correlation of observational errors. In contrast to the clear dependence on  $\Delta \log I_e$  shown here, Trager et al. (2000) did not find any dependence of the age- $[\text{Fe}/\text{H}]$  anti-correlation on  $I_e$  but in fact found that there was no improvement in statistical fits of age or  $[\text{Fe}/\text{H}]$  when  $I_e$  was included with  $\sigma$  as one of the fitting parameters. This is probably because they were fitting against absolute  $I_e$  rather than  $\Delta \log I_e$  at fixed  $\sigma$  and  $R_e$  (recall that Figure 6 shows only very weak dependence of stellar population parameters on absolute  $\log I_e$ ). There is a message here for multi-parameter fits in general: to detect a relation versus a residual in a higher-dimensional space, it is necessary to fit against that residual explicitly; the variation may remain concealed when using the parent coordinate alone.

A similar anti-correlation between residuals in age and Mg abundance is apparent in Figure 11b. Again, the anti-correlation is strongly dependent on  $\Delta \log I_e$ . The

strength of the anti-correlation is weaker than the age- $[\text{Fe}/\text{H}]$  trend at fixed  $\sigma$  ( $\Delta[\text{Mg}/\text{H}] \propto -0.4\Delta(\log \text{age})$ ). This is consistent with the fact that Figure 4 shows less spread in  $[\text{Mg}/\text{H}]$  at fixed  $\sigma$  than in  $[\text{Fe}/\text{H}]$ . In addition to the total abundance of Mg at fixed  $\sigma$ , there are also systematic variations in the abundance ratio  $[\text{Mg}/\text{Fe}]$ . Figure 11c shows that  $[\text{Mg}/\text{Fe}]$  is anti-correlated with  $[\text{Fe}/\text{H}]$  at fixed  $\sigma$ , so that Fe-poor galaxies are more Mg-enhanced than their Fe-rich counterparts. As with age,  $[\text{Fe}/\text{H}]$ , and  $[\text{Mg}/\text{H}]$ , residuals from the  $\log \sigma$ - $[\text{Mg}/\text{Fe}]$  relation are correlated with  $\Delta \log I_e$ . Finally, Figure 11d shows that residuals in age are positively correlated with residuals in  $[\text{Mg}/\text{Fe}]$ , such that older galaxies are more Mg-enhanced than younger galaxies at the same  $\sigma$ . The statistical errors in age and  $[\text{Mg}/\text{Fe}]$  are uncorrelated (i.e., the error ellipses in panel d are horizontal) because, although age errors in the stellar population modelling process affect individual abundance measurements, abundance ratio determinations are robust to modest age errors.

In summary, there are correlations between the residuals from all of the various stellar population parameter trends with  $\sigma$ . These depend on  $\Delta \log I_e$  such that high-SB galaxies have younger ages, higher  $[\text{Fe}/\text{H}]$ , higher  $[\text{Mg}/\text{H}]$ , and lower  $[\text{Mg}/\text{Fe}]$  than low-SB galaxies with the same  $\sigma$  and  $R_e$ . These trends are similar to those reported in Paper I, where more luminous galaxies (those

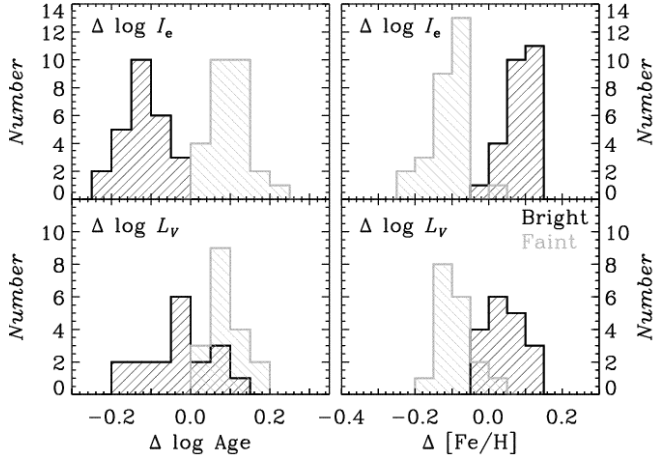


FIG. 12.— Comparison of the discriminatory power of  $\Delta \log L_V$  and  $\Delta \log I_e$  for distinguishing different galaxy stellar populations at fixed  $\sigma$ . *Top*: Black (gray) histograms show the age and [Fe/H] distributions for “brighter” (“fainter”) galaxies, as identified by  $\Delta \log I_e$ . Galaxies with differing stellar populations are well-separated by the  $\Delta \log I_e$  criterion. *Bottom*: Black (gray) histograms show the age and [Fe/H] distributions for brighter (fainter) galaxies, as identified by  $\Delta \log L_V$  for the same sample of galaxies (data from Paper I). The  $\Delta \log L_V$  criterion also does a reasonable job of separating galaxies with different stellar populations, but overall provides less clear separation than  $\Delta \log I_e$ : the galaxies in each bin are more mixed (in age and [Fe/H]) and the total spread between the peaks (in both age and [Fe/H]) is smaller. Thus  $\Delta \log I_e$  is preferable for distinguishing galaxies with different star formation histories at fixed  $\sigma$ .

with higher  $\Delta \log L_V$ ) were similarly younger, more Fe-rich, more Mg-rich, and with lower [Mg/Fe] with respect to less luminous galaxies at the same  $\sigma$ .

In this context, one can ask whether  $\Delta \log L_V$  (from Paper I) or  $\Delta \log I_e$  (from this work) is the better discriminator of differing stellar populations at fixed  $\sigma$  (i.e., does the best job of separating galaxies with differing star formation histories from one another). Figure 12 compares the discriminatory power of binning galaxies by  $\Delta \log I_e$  (as in this analysis) versus binning by  $\Delta \log L_V$  (as in Paper I). In each analysis, galaxies were divided into “bright”, “medium”, and “faint” bins at fixed  $\sigma$ , based either on  $\Delta \log I_e$  or on  $\Delta \log L_V$ . The “medium” brightness bins are not included in Figure 12 because the “bright” and “faint” bins best illustrate the total spread in stellar population properties.

The top panels of Figure 12 show histograms of the residuals from the age- $\sigma$  and [Fe/H]- $\sigma$  relations based on the  $\Delta \log I_e$  used in this analysis. Sorting galaxies by  $\Delta \log I_e$  does an excellent job of separating out galaxies with differing star formation histories: the galaxies with the high-SB (black histograms) have the youngest mean ages and the highest [Fe/H], while those with the low-SB (gray histograms) have the oldest mean ages and lower [Fe/H]. The separation between the two populations is very clear. If  $\Delta \log L_V$  is used to bin galaxies at fixed  $\sigma$  (lower panels), the results are generally similar. However, the differences between high and low peaks are larger in both cases with  $\Delta \log I_e$  than with  $\Delta \log L_V$ . This is as expected since  $\Delta \log I_e$  is a “pure” stellar population measure whereas  $\Delta \log L_V$  also contains informa-

tion from  $\Delta \log R_e$  (at fixed  $\sigma$ ). As illustrated in Figures 7–10,  $\Delta \log R_e$  is irrelevant to stellar population parameters, and thus its presence in  $\Delta \log L_V$  serves only to dilute the information in that quantity. To conclude, if one is searching for the best way to identify the youngest (or most Fe-rich) galaxies at a given  $\sigma$ ,  $\Delta \log I_e$  is a better discriminant than  $\Delta \log L_V$ . There may be cases where radii are not measurable or not available for individual galaxies, particularly in high redshift surveys, in which case  $\Delta \log L_V$  still provides reasonable discriminatory power.

The stellar population maps discussed in §4.2 showed very little variation in stellar population properties as a function of  $R_e$  at fixed  $\sigma$ . A direct comparison of stellar population residuals and their dependence on  $R_e$  is shown in Figure 13. Here, stellar population residuals are shown as a function of  $\Delta \log R_e$ , where  $\Delta \log R_e$  is defined as the difference between the median  $\log R_e$  for each bin and the median  $\log R_e$  for *all* galaxies in the same  $\sigma$  range. The weak dependence of  $R_e$  on  $\sigma$  has therefore been removed, highlighting the effect of  $R_e$  alone. It is clear that the stellar population residuals are unrelated to galaxy size at fixed  $\sigma$ .

This is an interesting and perhaps surprising result. The total  $M_{dyn}$  scales as  $\sigma^2 R_e$ . Thus, if the fundamental galaxy property driving stellar population variations were galaxy mass, we would expect residuals from  $\sigma$  trends to correlate with  $R_e$  as well as with  $\sigma$ . If this were the case, the contours of age, [Fe/H], [Mg/H], and [Mg/Fe] in Figures 7–10 would follow the dashed lines of  $M_{dyn}$ . Instead, lines of constant population properties run nearly vertically in those figures, and the residuals shown here in Figure 13 are completely independent of  $R_e$ . This suggests that it is in fact  $\sigma$  and *not* total mass that is fundamentally related to the galaxy star formation history. The emerging generation of cosmological models, including predictions for stellar velocity dispersions, may be able to shed light on the different evolutionary histories of galaxies with the same total  $M_{dyn}$  but different values of  $\sigma$  (and vice versa).

Taken together, these results indicate that  $\sigma$  is the primary structural parameter controlling stellar population variations, and therefore the primary predictor of a galaxy’s past star formation history. Indeed,  $\sigma$  appears to be more fundamental than total mass, because residuals from the mean trends between  $\sigma$  and the various stellar population properties do not correlate with  $R_e$ . At fixed  $\sigma$ , there are additional, genuine correlations between stellar population parameters which seem to depend strongly on  $\Delta \log I_e$  such that high-SB galaxies are younger, more Fe-rich, and more Mg-rich, but with less enhanced [Mg/Fe] than typical galaxies at the same  $\sigma$ . Conversely, low-SB galaxies at the same  $\sigma$  are older, Fe-poor, Mg-poor, and show significantly enhanced [Mg/Fe]. These correlations provide strong constraints on cosmological models of galaxy formation and are an important tool for understanding past star formation histories of early-type galaxies. The implications for galaxy star formation histories will be discussed in detail in Paper III.

#### 4.4. Can the Observed Variation in Stellar Populations Be Caused by Measurement Errors in the FP Parameters?

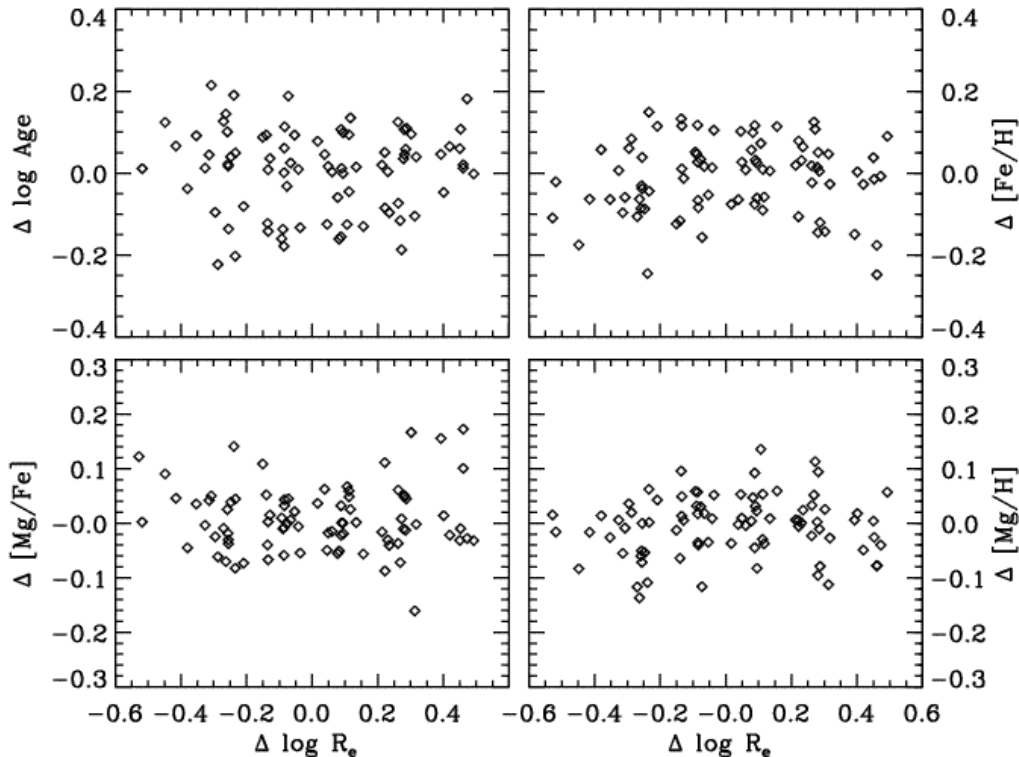


FIG. 13.— Residuals from the mean stellar population trends with  $\sigma$  as a function of residuals in  $R_e$ . The residual  $\Delta \log R_e$  is computed from the median  $\log R_e$  value for each bin by subtracting the median  $\log R_e$  for *all* galaxies at the corresponding  $\sigma$  (i.e., removing the weak dependence of  $R_e$  on  $\sigma$ ). As expected from Figures 7–10, there is no correlation between any stellar population residual and  $\Delta \log R_e$ .

We have argued that, because the thickness of the FP in  $I_e$  is strongly correlated with stellar population variations, that the thickness of the plane must be real, rather than merely scatter due to observational errors. But before accepting this, it is worth checking that the observed stellar population trends cannot be *caused* by observational errors in the FP parameters. It is obvious that, if the thickness of the FP in the  $I_e$  dimension is due to errors in  $I_e$  itself, we should not see any trends with  $I_e$ . What about thickness in  $I_e$  that is due to errors in  $R_e$  and/or  $\sigma$  that “scatter” galaxies into a different  $I_e$  bin?

The slope of the FP indicates that higher  $\sigma$  galaxies tend to have higher  $I_e$ , thus galaxies with observed high  $I_e$  should be galaxies that have “scattered” in from high  $\sigma$  (i.e., galaxies for which  $\sigma$  has been underestimated). However, the galaxies scattered in from higher  $\sigma$  would have older ages and higher [Mg/Fe], which is opposite to the observed trend with  $\Delta \log I_e$ . It is therefore not possible that errors in  $\sigma$  could produce the observed trends in  $I_e$  and stellar population properties. In the case of  $R_e$ ,  $I_e$  is calculated as  $I_e = L/2\pi R_e^2$  so overestimating  $R_e$  will result in underestimating  $I_e$ . However, we have shown that stellar populations do not depend on  $R_e$  and thus errors in measuring  $R_e$  cannot explain the observed stellar population variations as a function of  $I_e$ . This leads to the conclusion that the thickness of the FP in  $I_e$  is intrinsic to the galaxy population, rather than an artifact of measurement error, and therefore that the observed stellar population variation with  $\Delta \log I_e$  is likewise real.

## 5. DISCUSSION

We have seen that, while stellar population properties and therefore galaxy star formation histories vary substantially with  $\sigma$ , they do not vary with  $R_e$ . Although this is not a new result (cf., Trager et al. 2000), it is somewhat perplexing, as it implies that  $\sigma$ , and *not total galaxy mass*, is the better predictor of galaxy star formation history. In the literature,  $\sigma$  is often used as a proxy for galaxy mass in stellar population analyses; authors routinely refer to galaxies with higher  $\sigma$  as “more massive”, implying that the two parameters are interchangeable. Various authors have studied stellar population variations as function of  $\sigma$  (e.g., Trager et al. 2000; Bernardi et al. 2003b; Thomas et al. 2005; Smith et al. 2008b), as functions of  $M_*$ , (e.g., Gallazzi et al. 2005), and as functions of  $L$  (e.g., Kuntschner & Davies 1998; Terlevich & Forbes 2002). Thomas et al. (2005) in fact convert between  $\sigma$  and  $M_*$  using the mean relation between the two and present results for stellar population parameters as functions of either.

Comparisons between all these works are somewhat confusing and do not, at first glance, appear to give consistent results, particularly when addressing age variations in galaxies. This is in part because, although  $\sigma$ ,  $M_*$ , and  $L$  are all highly correlated, they are not exactly the same. It appears that stellar populations vary not only with  $\sigma$ , but that at fixed  $\sigma$ , they vary systematically with the residuals from the mean  $\sigma$ – $L$  relation (as shown in Paper I), so that stellar population trends with  $\sigma$  look significantly different from trends with  $L$ . (Trends as a function of  $M_*$  are very similar to trends with  $L$ , as  $M_*/L$  varies little among these galaxies.) We argue in



Paper I that the trends with  $\sigma$  are more fundamental and that tracking stellar population variations with  $L$  is not a good proxy for studying them as a function of  $\sigma$ . The work presented here suggests that  $M_{dyn}$  is also not a good proxy for  $\sigma$  and confirms that  $\sigma$  is the best predictor of galaxy star formation histories. Models of galaxy formation must reproduce this dependence on  $\sigma$ .

Simulations of galaxy mergers offer some insight into why  $R_e$  might be unrelated to galaxy stellar populations. Robertson et al. (2006) present a series of dissipational galaxy merger simulations, along with a study of how various properties of the mergers affect the FP parameters of the resulting merger remnant galaxies. They find that the final  $R_e$  of the merger remnant depends strongly on the orientation of the initial galaxy orbits and the total angular momentum of the pre-merger system. Different initial orientations produce a factor of two variation in the resulting  $R_e$  of the merger remnant for re-simulations of collisions between identical progenitor galaxies. The stellar populations of a galaxy should be independent of galaxy orbit angular momentum and orientation before a merger; therefore dissipational mergers will tend to decouple the remnant  $R_e$  from any original relation between galaxy size and star formation history, should one exist.

Subsequent dissipationless merging of early-type galaxies will also tend to further scatter galaxies in  $R_e$ , while having only a small effect on  $\sigma$  and presumably having no effect on the stellar population of the galaxy. Simulations of dissipationless mergers between equal-mass systems by Boylan-Kolchin et al. (2005) result in remnants with  $R_e$  around 70% (0.23 dex) higher than the pre-merger systems, while the  $\sigma$  of the remnant differs by < 20% (0.06 dex) from the pre-merger system. Thus equal-mass dissipationless merging modifies  $R_e$  without create major changes in  $\sigma$  or the stellar populations of galaxies, thereby scrambling any pre-existing correlations.

These merger simulations suggest that any initial correlation between galaxy size and star formation history will be erased through extensive merging. Gas-rich dissipational mergers will produce remnants whose radii depend strongly on the orbital orientations of the progenitors, scrambling any initial size-dependence. Variable quantities of subsequent gas-poor dissipationless mergers, which change  $R_e$  but have only minor effects on  $\sigma$  and no effect on the stellar population, will further serve to erase any original stellar population dependence on  $R_e$ .

## 6. CONCLUSIONS

We have identified a sample of  $\sim 16,000$  early-type galaxies from the SDSS spectroscopic Main Galaxy Sample to study star formation histories in FP space. Bins of similar galaxies are defined along the FP in  $\log \sigma$  and  $\log R_e$ , and through the thickness of the FP in  $\Delta \log I_e$ . Spectra of the galaxies in each bin are coadded to produce a set of high  $S/N$  mean spectra that span the FP. The mean spectra are compared with the stellar population models of Schiavon (2007) using the automated IDL code *EZ\_Ages* (Graves & Schiavon 2008), which determines the mean luminosity-weighted age, abundances  $[\text{Fe}/\text{H}]$ ,  $[\text{Mg}/\text{H}]$ , and the abundance ratio  $[\text{Mg}/\text{Fe}]$  for each stacked spectrum. This allows us to study the variations of stellar populations throughout FP space.

The star formation histories of early-type galaxies are found to form a two-parameter family. Interestingly, these two parameters correlate with  $\sigma$  and with  $\Delta \log I_e$  but not with  $R_e$ . In other words, the two-parameter family of star formation histories vary across one dimension of the FP and through the thickness of the FP, but do not seem to vary with the second dimension across the FP. A detailed summary of our results follows.

1. Stellar population age,  $[\text{Fe}/\text{H}]$ ,  $[\text{Mg}/\text{H}]$ , and  $[\text{Mg}/\text{Fe}]$  all increase with increasing galaxy  $\sigma$ . This implies a close relationship between  $\sigma$  and the star formation history of a galaxy. Age and  $[\text{Fe}/\text{H}]$  show substantial spreads at fixed  $\sigma$ , while  $[\text{Mg}/\text{Fe}]$  and  $[\text{Mg}/\text{H}]$  vary less. The relation between  $\sigma$  and  $[\text{Mg}/\text{H}]$  is particularly strong and tight, showing very little spread at high  $\sigma$  and only modest spread at low  $\sigma$ .
2. Stellar population properties are independent of galaxy size,  $R_e$ . This suggests that  $\sigma$  is a better predictor of the star formation history of a galaxy than total mass since dynamical mass scales as  $M_{dyn} \propto \sigma^2 R_e$ . This can be understood in the context of merger-driven galaxy formation, where  $R_e$  is strongly affected by the initial orbital conditions of the merging galaxies and may be subsequently further altered by dissipationless merging (which does not affect the stellar population).
3. At fixed  $\sigma$  and  $R_e$ , stellar populations vary substantially with surface brightness residuals from the FP, parameterized by  $\Delta \log I_e$ . This has a number of implications. Firstly, the thickness of the FP is real rather than merely due to measurement error. Furthermore, the thickness of the FP represents an age sequence, such that galaxies with higher surface brightness than the midplane of the FP have younger ages, while galaxies with lower surface brightness than the midplane have older ages. This result is in agreement with the work of Forbes et al. (1998), Terlevich & Forbes (2002), and Treu et al. (2005b).
4. In addition to age variations through the thickness of the FP, there are corresponding variations in all other stellar population properties studied here. The variations in age,  $[\text{Fe}/\text{H}]$ ,  $[\text{Mg}/\text{H}]$ , and  $[\text{Mg}/\text{Fe}]$  at fixed  $\sigma$  are correlated with one another such that the galaxies with higher surface brightness than the FP midplane are younger, significantly more Fe-rich, only slightly more Mg-rich, and have lower  $[\text{Mg}/\text{Fe}]$  than their counterparts on the FP. Similarly, galaxies with lower surface brightness than the FP midplane are older, less Fe-rich, slightly less Mg-rich, and have substantially enhanced  $[\text{Mg}/\text{Fe}]$  relative to their counterparts on the FP. The general age-metallicity anti-correlation is consistent with previous work by Trager et al. (2000) and Smith et al. (2008b). Although these co-variations are in the directions of the correlated errors in stellar population modelling, neither the statistical errors nor the known systematic errors in the modelling process can explain the variations, strongly suggesting that they are real effects.

5. The variations with  $\Delta \log I_e$  at fixed  $\sigma$  and  $R_e$  demonstrated in this analysis are consistent with the results of Paper I, which showed similar stellar population variations with  $\Delta \log L_V$  at fixed  $\sigma$ . However, the FP residual  $\Delta \log I_e$  does a somewhat better job of distinguishing young Fe-rich populations from old Fe-poor populations at the same  $\sigma$  and is thus preferable to  $\Delta \log L_V$  for studying variations in the star formation histories of early-type galaxies.

This work demonstrates that the stellar populations of early-type galaxy form a two-parameter family. This two-parameter family maps onto a cross-section through the FP. Paper III in this series will explicitly quantify this mapping, as well as translating the derived stellar population parameters into model star formation histories.

The authors would like to thank Arjen van der Wel for providing effective radius measurements based on GALFIT photometry as a check on the SDSS pipeline radii, and Renbin Yan for providing the emission line measure-

ments used to identify the sample of early-type galaxies used here. This work was supported by National Science Foundation grant AST 05-07483.

Funding for the creation and distribution of the SDSS Archive has been provided by the Alfred P. Sloan Foundation, the Participating Institutions, the National Aeronautics and Space Administration, the National Science Foundation, the US Department of Energy, the Japanese Monbukagakusho, and the Max-Planck Society. The SDSS Web site is <http://www.sdss.org/>.

The SDSS is managed by the Astrophysical Research Consortium (ARC) for the Participating Institutions. The Participating Institutions are the University of Chicago, Fermilab, the Institute for Advanced Study, the Japan Participation Group, the Johns Hopkins University, the Korean Scientist Group, Los Alamos National Laboratory, the Max-Planck-Institute for Astronomy (MPIA), the Max-Planck-Institute for Astrophysics (MPA), New Mexico State University, University of Pittsburgh, University of Portsmouth, Princeton University, the United States Naval Observatory, and the University of Washington.

## APPENDIX FROSTING MODELS

Section 4.3 showed that correlated statistical errors cannot account for the co-variation of stellar population properties with  $\Delta \log I_e$  at fixed  $\sigma$ . The younger ages observed for high-SB galaxies are genuine variations, in agreement with the results of Forbes et al. (1998). However, the stellar population models used in this work are single-burst models. Because young stars are luminous and contribute disproportionately to integrated galaxy light and Balmer absorption line strengths, a small population of young stars can skew the “mean” age to younger values than a true, mass-weighted mean age. The effect is largest when the age difference between sub-populations is large compared to the mean stellar age, so that the youngest age measurements in our data are likely to be somewhat too young. Determinations of age and  $[\text{Fe}/\text{H}]$  from absorption indices are anti-correlated, so a young component would not only skew the mean age to younger values but should also skew the measured  $[\text{Fe}/\text{H}]$  to higher values. Because  $[\text{Mg}/\text{Fe}]$  is an abundance ratio, it is relatively insensitive to the correlated errors in age and  $[\text{Fe}/\text{H}]$  (see Figure 3 of Graves & Schiavon (2008)). The abundance  $[\text{Mg}/\text{H}]$  is calculated as  $[\text{Fe}/\text{H}] + [\text{Mg}/\text{Fe}]$ , so errors in  $[\text{Fe}/\text{H}]$  will translate directly into comparable errors in  $[\text{Mg}/\text{H}]$ .

Figure 14 shows absorption line strength predictions for  $\text{H}\beta$  and  $\langle \text{Fe} \rangle$  from stellar population models. The black grid shows a set of single-burst models from Schiavon (2007) with solar abundance ratios. Solid lines indicate lines of constant  $[\text{Fe}/\text{H}]$ , while dotted lines indicate lines of constant age, as labelled in the figure. In addition to the grid of single burst models, two different frosting models are shown. The dark gray line shows the effect of adding a burst with age 1.2 Gyr to an underlying stellar population with an age of 14.1 Gyr. Both the old and young population components have  $[\text{Fe}/\text{H}] = -0.4$ . Diamonds indicate the fraction of galaxy light contributed by the young burst, starting at the bottom at 0% and increasing in increments of 5% moving upward along the line. This line shows the trajectory in  $\text{H}\beta$ - $\langle \text{Fe} \rangle$  space produced by adding young bursts at the same  $[\text{Fe}/\text{H}]$  to an underlying old population. Though this model is computed for a burst, the direction traced by adding a *range* of younger stars would be the same or tilted even more strongly to the left. The light gray line with “X” symbols shows a similar frosting model, but here the young 1.2 Gyr burst is four times more Fe-rich than the underlying old population, with  $[\text{Fe}/\text{H}] = +0.2$ .

The colored points show the data from our stacked galaxy spectra. Different colors represent the different bins in  $\sigma$ , with purple indicating the lowest- $\sigma$  bin and red indicating the highest- $\sigma$  bin. At each value of  $\sigma$ , the three circles indicate the three bins in  $\Delta \log I_e$ , with the smallest circle showing the low-SB bin and the largest circle showing the high-SB bin. The bins have been averaged over  $R_e$ .

It is interesting that the slopes between the low-SB and midplane bins (small and medium circles) are substantially different from those between the midplane and high-SB bins (medium and large circles). Comparing first the low-SB and midplane bins, it is clear that the differences between low-SB and midplane galaxies cannot be explained at all by a small frosting of younger stars at the same  $[\text{Fe}/\text{H}]$ . The same-Fe frosting model (dark gray line with diamonds) is nearly orthogonal to the change in  $\text{H}\beta$ - $\langle \text{Fe} \rangle$  space between the low-SB and midplane bins. Even adding a frosting population with four times larger Fe abundance (light gray lines with exes) does not come close to explaining the  $\langle \text{Fe} \rangle$  line strength differences between the low-SB and midplane galaxies. The low-SB galaxies must have genuinely lower values of  $[\text{Fe}/\text{H}]$  than the galaxies at the FP midplane, as well as having older ages.

Line strengths differences between the midplane galaxies and the high-SB galaxies are more similar to the  $\text{H}\beta$ - $\langle \text{Fe} \rangle$  trajectories expected for frosting models, particularly for low- $\sigma$  galaxies. At high  $\sigma$ , neither the constant  $[\text{Fe}/\text{H}]$  nor

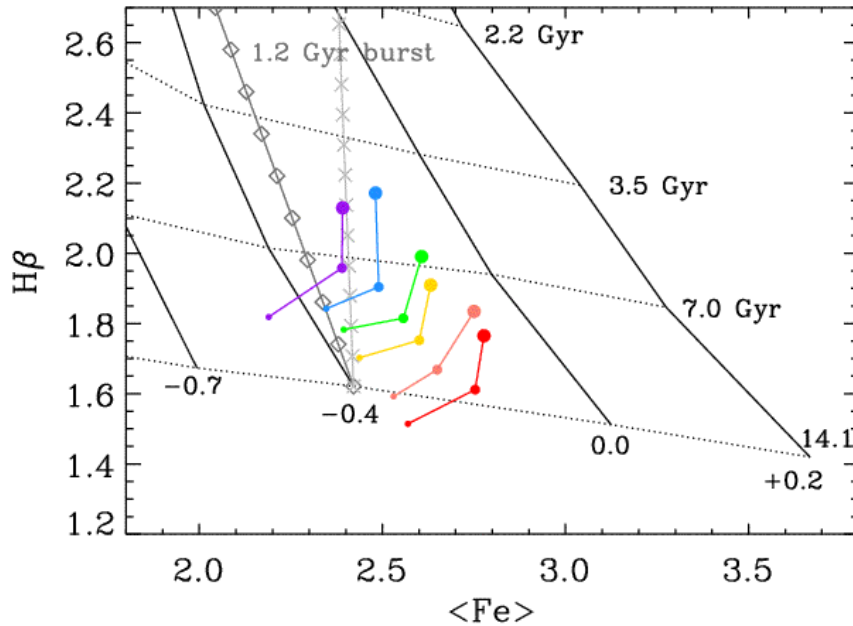


FIG. 14.— Comparing observed index variations with two-burst “frosting” stellar population models. The black grid shows solar-ratio single burst models from Schiavon (2007). Solid lines indicate lines of constant  $[\text{Fe}/\text{H}]$ , while dotted lines indicate lines of constant age, as labelled. The dark gray trajectory shows the effect of adding a 1.2 Gyr burst with  $[\text{Fe}/\text{H}] = -0.4$  to an underlying 14.1 Gyr old population with the same  $[\text{Fe}/\text{H}]$ . Diamonds indicate the fraction of the galaxy light at  $\sim 5000 \text{ \AA}$  contributed by the young population, starting from 0% at the bottom and increasing in increments of 5% to 45% at the top of the diagram. The light gray trajectory shows the effect of adding a 1.2 Gyr burst with four times larger Fe abundance ( $[\text{Fe}/\text{H}] = +0.2$ ) to the underlying 14.1 Gyr population. “X”s indicate the fraction of light contributed by the young Fe-rich population in increments of 5%. The indices measured in our stacked SDSS spectra are shown as colored points, with purple, blue, green, gold, orange, and red indicating the lowest through highest  $\sigma$  bins, respectively. Small, medium, and large circles indicate the low-SB, midplane, and high-SB bins in  $\Delta \log I_e$ , respectively. Differences between the low-SB and midplane bins cannot be produced merely by adding a young subpopulation of stars—a genuinely higher  $[\text{Fe}/\text{H}]$  population is required. Differences between the midplane and high-SB bins are compatible with a young subpopulation at the same  $[\text{Fe}/\text{H}]$  for the lowest  $\sigma$  bin only—higher  $\sigma$  bins also require a genuinely higher  $[\text{Fe}/\text{H}]$  population. The observed anti-correlation between mean age and  $[\text{Fe}/\text{H}]$  at fixed  $\sigma$  therefore reflects genuine differences in the stellar population abundances and cannot be caused solely by systematic effects from using single burst stellar population models.

the Fe-rich frosting models can account for the observed increases in  $\langle \text{Fe} \rangle$  in the high-SB galaxies. For the lowest  $\sigma$  bin, the difference between the midplane galaxies and the high-SB galaxies is consistent with a  $\sim 5\%$  frosting of young stars at similar  $[\text{Fe}/\text{H}]$  to the underlying population—no genuine difference in  $[\text{Fe}/\text{H}]$  is needed to explain the data. However, the difference in  $[\text{Fe}/\text{H}]$  inferred from assuming a single burst population is only 0.04 dex. This indicates that the simplifying assumption of a single burst population only biases the estimated  $[\text{Fe}/\text{H}]$  by a small amount for the high-SB, lowest- $\sigma$  galaxies, where the bias is strongest. This small bias in the measured  $[\text{Fe}/\text{H}]$  will translate into a similarly small bias in  $[\text{Mg}/\text{H}]$ .

In general, a small frosting of younger stars, while adequate to explain the observed differences in stellar population ages at fixed  $\sigma$ , cannot also produce the observed variation in  $[\text{Fe}/\text{H}]$  and  $[\text{Mg}/\text{H}]$ . The variation in  $\langle \text{Fe} \rangle$  linestrength at fixed  $\sigma$  requires a real variation in  $[\text{Fe}/\text{H}]$ . Thus the variations in observed abundance patterns at fixed  $\sigma$  must be due to genuine abundance differences between the galaxies, rather than an artifact of the modelling process for the younger galaxies.

#### REFERENCES

- Adelman-McCarthy, J. K., et al. 2006, *ApJS*, 162, 38  
Adelman-McCarthy, J. K. f. 2008, *ApJS*, 175, 297  
Bender, R., Burstein, D., & Faber, S. M. 1992, *ApJ*, 399, 462  
Bernardi, M., et al. 2003a, *AJ*, 125, 1866  
—, 2003b, *AJ*, 125, 1882  
Blanton, M. R., et al. 2003, *AJ*, 125, 2348  
Blanton, M. R., et al. 2005, *AJ*, 129, 2562  
Boylan-Kolchin, M., Ma, C.-P., & Quataert, E. 2005, *MNRAS*, 362, 184  
Cardiel, N., Gorgas, J., Cenarro, J., & Gonzalez, J. J. 1998, *A&AS*, 127, 597  
Djorgovski, S. & Davis, M. 1987, *ApJ*, 313, 59  
Dressler, A., Lynden-Bell, D., Burstein, D., Davies, R. L., Faber, S. M., Terlevich, R., & Wegner, G. 1987, *ApJ*, 313, 42  
Faber, S. M., Dressler, A., Davies, R. L., Burstein, D., & Lynden-Bell, D. 1987, in *Nearly Normal Galaxies. From the Planck Time to the Present*, ed. S. M. Faber, 175–183  
Fisher, D. B. & Drory, N. 2008, *AJ*, 136, 773  
Forbes, D. A., Ponman, T. J., & Brown, R. J. N. 1998, *ApJ*, 508, L43  
Gallazzi, A., Charlot, S., Brinchmann, J., White, S. D. M., & Tremonti, C. A. 2005, *MNRAS*, 362, 41  
Graves, G. J., Faber, S. M., & Schiavon, R. P. 2009, *ApJ*, 693, 486

- Graves, G. J., Faber, S. M., Schiavon, R. P., & Yan, R. 2007, *ApJ*, 671, 243
- Graves, G. J. & Schiavon, R. P. 2008, *ApJS*, 177, 446
- Jørgensen, I., Chiboucas, K., Flint, K., Bergmann, M., Barr, J., & Davies, R. 2006, *ApJ*, 639, L9
- Jørgensen, I., Franx, M., & Kjaergaard, P. 1996, *MNRAS*, 280, 167
- Kauffmann, G., et al. 2003, *MNRAS*, 346, 1055
- Kormendy, J. & Fisher, D. B. 2008, in *Astronomical Society of the Pacific Conference Series*, Vol. 396, *Astronomical Society of the Pacific Conference Series*, ed. J. G. Funes & E. M. Corsini, 297
- Kuntschner, H. & Davies, R. L. 1998, *MNRAS*, 295, L29
- Nelan, J. E., Smith, R. J., Hudson, M. J., Wegner, G. A., Lucey, J. R., Moore, S. A. W., Quinney, S. J., & Suntzeff, N. B. 2005, *ApJ*, 632, 137
- Peng, C. Y., Ho, L. C., Impey, C. D., & Rix, H.-W. 2002, *AJ*, 124, 266
- Robertson, B., Cox, T. J., Hernquist, L., Franx, M., Hopkins, P. F., Martini, P., & Springel, V. 2006, *ApJ*, 641, 21
- Schawinski, K., Thomas, D., Sarzi, M., Maraston, C., Kaviraj, S., Joo, S.-J., Yi, S. K., & Silk, J. 2007, *MNRAS*, 382, 1415
- Schiavon, R. P. 2007, *ApJS*, 171, 146
- Sersic, J. L. 1968, *Atlas de galaxias australes* (Cordoba, Argentina: Observatorio Astronomico, 1968)
- Smith, R. J., Lucey, J. R., & Hudson, M. J. 2007a, *MNRAS*, 381, 1035
- . 2008b, in *Proc. of IAUS 245, Formation and Evolution of Galaxy Bulges*, p. 411-414, arXiv:0712.0274
- Strauss, M. A., et al. 2002, *AJ*, 124, 1810
- Terlevich, A. I. & Forbes, D. A. 2002, *MNRAS*, 330, 547
- Thomas, D., Maraston, C., Bender, R., & Mendes de Oliveira, C. 2005, *ApJ*, 621, 673
- Trager, S. C., Faber, S. M., Worthey, G., & González, J. J. 2000, *AJ*, 120, 165
- Treu, T., Ellis, R. S., Liao, T. X., & van Dokkum, P. G. 2005a, *ApJ*, 622, L5
- Treu, T., et al. 2005b, *ApJ*, 633, 174
- van der Wel, A., Franx, M., van Dokkum, P. G., & Rix, H.-W. 2004, *ApJ*, 601, L5
- van der Wel, A., Franx, M., van Dokkum, P. G., Rix, H.-W., Illingworth, G. D., & Rosati, P. 2005, *ApJ*, 631, 145
- Worthey, G., Faber, S. M., Gonzalez, J. J., & Burstein, D. 1994, *ApJS*, 94, 687
- Worthey, G. & Ottaviani, D. L. 1997, *ApJS*, 111, 377
- Worthey, G., Trager, S. C., & Faber, S. M. 1995, in *Astronomical Society of the Pacific Conference Series*, Vol. 86, *Fresh Views of Elliptical Galaxies*, ed. A. Buzzoni, A. Renzini, & A. Serrano, 203
- Yan, R., Newman, J. A., Faber, S. M., Konidaris, N., Koo, D., & Davis, M. 2006, *ApJ*, 648, 281
- York, D. G., et al. 2000, *AJ*, 120, 1579

TABLE 1  
PROPERTIES OF GALAXY BINS AND STACKED SPECTRA

	$\sigma$ bin* (km s <sup>-1</sup> )	$R_e$ bin* (kpc)	$I_e$ bin* ( $L_\odot$ pc <sup>-2</sup> )	Median log $\sigma$ (km s <sup>-1</sup> )	Median log $R_e$ (kpc)	Median $\Delta$ log $I_e$ ( $L_\odot$ pc <sup>-2</sup> )	Median log $I_e$ ( $L_\odot$ pc <sup>-2</sup> )	Number <sup>†</sup>	$S/N^\dagger$ ( $\text{\AA}^{-1}$ )
1	1.86 < $\sigma$ < 2.00	-0.1 < $R_e$ < 0.1	-0.3 < $\Delta I_e$ < -0.1	1.96	0.05	-0.17	2.60	33	85
2			-0.1 < $\Delta I_e$ < 0.1	1.94	0.04	0.01	2.78	86	158
3			0.1 < $\Delta I_e$ < 0.3	1.94	0.05	0.19	2.95	39	115
4		0.1 < $R_e$ < 0.3	-0.3 < $\Delta I_e$ < -0.1	1.95	0.21	-0.17	2.37	89	154
5			-0.1 < $\Delta I_e$ < 0.1	1.95	0.22	0.00	2.55	276	273
6			0.1 < $\Delta I_e$ < 0.3	1.94	0.20	0.15	2.72	133	214
7		0.3 < $R_e$ < 0.5	-0.3 < $\Delta I_e$ < -0.1	1.95	0.40	-0.16	2.15	119	159
8			-0.1 < $\Delta I_e$ < 0.1	1.94	0.40	-0.01	2.32	263	259
9			0.1 < $\Delta I_e$ < 0.3	1.95	0.39	0.14	2.48	65	154
10		0.5 < $R_e$ < 0.7	-0.3 < $\Delta I_e$ < -0.1	1.96	0.55	-0.17	1.97	36	80
11			-0.1 < $\Delta I_e$ < 0.1	1.94	0.57	-0.01	2.10	75	152
12			0.1 < $\Delta I_e$ < 0.3	1.93	0.55	0.13	2.26	23	89
13		0.7 < $R_e$ < 0.9	-0.3 < $\Delta I_e$ < -0.1	...	...	...	...	3	27
14			-0.1 < $\Delta I_e$ < 0.1	1.96	0.76	0.01	1.86	18	77
15			0.1 < $\Delta I_e$ < 0.3	...	...	...	...	5	41
16	2.00 < $\sigma$ < 2.09	-0.1 < $R_e$ < 0.1	-0.3 < $\Delta I_e$ < -0.1	2.05	0.03	-0.15	2.75	51	130
17			-0.1 < $\Delta I_e$ < 0.1	2.06	0.03	0.01	2.91	190	262
18			0.1 < $\Delta I_e$ < 0.3	2.06	0.00	0.15	3.09	73	180
19		0.1 < $R_e$ < 0.3	-0.3 < $\Delta I_e$ < -0.1	2.05	0.24	-0.15	2.50	157	207
20			-0.1 < $\Delta I_e$ < 0.1	2.06	0.21	-0.00	2.68	491	419
21			0.1 < $\Delta I_e$ < 0.3	2.05	0.20	0.15	2.86	108	225
22		0.3 < $R_e$ < 0.5	-0.3 < $\Delta I_e$ < -0.1	2.05	0.38	-0.15	2.30	186	224
23			-0.1 < $\Delta I_e$ < 0.1	2.05	0.38	-0.01	2.46	470	421
24			0.1 < $\Delta I_e$ < 0.3	2.06	0.38	0.15	2.65	93	221
25		0.5 < $R_e$ < 0.7	-0.3 < $\Delta I_e$ < -0.1	2.04	0.58	-0.17	2.04	64	120
26			-0.1 < $\Delta I_e$ < 0.1	2.06	0.57	-0.01	2.23	131	228
27			0.1 < $\Delta I_e$ < 0.3	2.06	0.56	0.15	2.44	20	119
28		0.7 < $R_e$ < 0.9	-0.3 < $\Delta I_e$ < -0.1	2.05	0.75	-0.12	1.83	12	56
29			-0.1 < $\Delta I_e$ < 0.1	2.06	0.74	0.02	2.02	24	101
30			0.1 < $\Delta I_e$ < 0.3	...	...	...	...	2	31
31	2.09 < $\sigma$ < 2.18	-0.1 < $R_e$ < 0.1	-0.3 < $\Delta I_e$ < -0.1	2.14	0.03	-0.16	2.84	100	190
32			-0.1 < $\Delta I_e$ < 0.1	2.14	0.04	0.00	3.00	348	371
33			0.1 < $\Delta I_e$ < 0.3	2.13	0.04	0.14	3.15	124	257
34		0.1 < $R_e$ < 0.3	-0.3 < $\Delta I_e$ < -0.1	2.13	0.21	-0.15	2.62	240	274
35			-0.1 < $\Delta I_e$ < 0.1	2.14	0.21	-0.00	2.78	817	594
36			0.1 < $\Delta I_e$ < 0.3	2.14	0.21	0.15	2.95	190	355
37		0.3 < $R_e$ < 0.5	-0.3 < $\Delta I_e$ < -0.1	2.13	0.38	-0.14	2.41	254	286
38			-0.1 < $\Delta I_e$ < 0.1	2.14	0.39	-0.00	2.56	785	644
39			0.1 < $\Delta I_e$ < 0.3	2.14	0.38	0.15	2.73	189	376
40		0.5 < $R_e$ < 0.7	-0.3 < $\Delta I_e$ < -0.1	2.14	0.58	-0.16	2.15	81	165
41			-0.1 < $\Delta I_e$ < 0.1	2.14	0.58	-0.00	2.33	343	439
42			0.1 < $\Delta I_e$ < 0.3	2.15	0.57	0.15	2.51	77	250
43		0.7 < $R_e$ < 0.9	-0.3 < $\Delta I_e$ < -0.1	2.14	0.76	-0.16	1.92	13	61
44			-0.1 < $\Delta I_e$ < 0.1	2.14	0.75	0.02	2.13	60	174
45			0.1 < $\Delta I_e$ < 0.3	2.15	0.79	0.13	2.24	24	132
46	2.18 < $\sigma$ < 2.27	-0.1 < $R_e$ < 0.1	-0.3 < $\Delta I_e$ < -0.1	2.23	0.04	-0.15	2.94	96	197
47			-0.1 < $\Delta I_e$ < 0.1	2.22	0.03	-0.01	3.10	302	387
48			0.1 < $\Delta I_e$ < 0.3	2.21	0.05	0.14	3.23	66	200
49		0.1 < $R_e$ < 0.3	-0.3 < $\Delta I_e$ < -0.1	2.22	0.21	-0.15	2.73	213	286
50			-0.1 < $\Delta I_e$ < 0.1	2.22	0.21	-0.01	2.88	679	630
51			0.1 < $\Delta I_e$ < 0.3	2.22	0.21	0.16	3.04	186	388
52		0.3 < $R_e$ < 0.5	-0.3 < $\Delta I_e$ < -0.1	2.22	0.39	-0.14	2.51	175	293
53			-0.1 < $\Delta I_e$ < 0.1	2.22	0.40	0.01	2.66	871	779
54			0.1 < $\Delta I_e$ < 0.3	2.23	0.39	0.15	2.82	227	463
55		0.5 < $R_e$ < 0.7	-0.3 < $\Delta I_e$ < -0.1	2.23	0.57	-0.15	2.29	81	192
56			-0.1 < $\Delta I_e$ < 0.1	2.23	0.58	0.01	2.44	555	637
57			0.1 < $\Delta I_e$ < 0.3	2.23	0.58	0.15	2.57	118	337
58		0.7 < $R_e$ < 0.9	-0.3 < $\Delta I_e$ < -0.1	2.21	0.74	-0.14	2.08	23	97
59			-0.1 < $\Delta I_e$ < 0.1	2.23	0.77	0.01	2.22	125	294
60			0.1 < $\Delta I_e$ < 0.3	2.25	0.75	0.14	2.38	36	183
61	2.27 < $\sigma$ < 2.36	-0.1 < $R_e$ < 0.1	-0.3 < $\Delta I_e$ < -0.1	2.31	0.00	-0.14	3.06	49	145
62			-0.1 < $\Delta I_e$ < 0.1	2.30	0.04	-0.03	3.19	127	273
63			0.1 < $\Delta I_e$ < 0.3	2.30	0.07	0.14	3.30	12	101
64		0.1 < $R_e$ < 0.3	-0.3 < $\Delta I_e$ < -0.1	2.30	0.19	-0.15	2.83	99	229
65			-0.1 < $\Delta I_e$ < 0.1	2.30	0.22	-0.02	2.95	278	451
66			0.1 < $\Delta I_e$ < 0.3	2.30	0.24	0.13	3.08	53	235
67		0.3 < $R_e$ < 0.5	-0.3 < $\Delta I_e$ < -0.1	2.31	0.37	-0.14	2.63	111	268
68			-0.1 < $\Delta I_e$ < 0.1	2.30	0.41	-0.01	2.73	527	688
69			0.1 < $\Delta I_e$ < 0.3	2.30	0.42	0.15	2.89	106	349
70		0.5 < $R_e$ < 0.7	-0.3 < $\Delta I_e$ < -0.1	2.32	0.56	-0.13	2.42	54	186
71			-0.1 < $\Delta I_e$ < 0.1	2.31	0.59	0.01	2.53	504	675
72			0.1 < $\Delta I_e$ < 0.3	2.31	0.61	0.14	2.65	161	422
73		0.7 < $R_e$ < 0.9	-0.3 < $\Delta I_e$ < -0.1	2.33	0.75	-0.12	2.19	11	89

TABLE 1  
PROPERTIES OF GALAXY BINS AND STACKED SPECTRA

74			$-0.1 < \Delta I_e < 0.1$	2.32	0.77	0.03	2.33	213	442
75			$0.1 < \Delta I_e < 0.3$	2.32	0.77	0.14	2.45	67	278
76	2.36 < $\sigma$ < 2.50	$-0.1 < R_e < 0.1$	$-0.3 < \Delta I_e < -0.1$	2.38	0.02	-0.15	3.17	19	100
77			$-0.1 < \Delta I_e < 0.1$	2.40	0.03	-0.03	3.28	37	168
78			$0.1 < \Delta I_e < 0.3$	...	...	...	...	3	53
79		$0.1 < R_e < 0.3$	$-0.3 < \Delta I_e < -0.1$	2.39	0.19	-0.15	2.94	32	149
80			$-0.1 < \Delta I_e < 0.1$	2.38	0.22	-0.03	3.03	71	266
81			$0.1 < \Delta I_e < 0.3$	...	...	...	...	3	58
82		$0.3 < R_e < 0.5$	$-0.3 < \Delta I_e < -0.1$	2.38	0.40	-0.13	2.68	35	170
83			$-0.1 < \Delta I_e < 0.1$	2.39	0.42	-0.01	2.82	149	408
84			$0.1 < \Delta I_e < 0.3$	2.37	0.41	0.14	2.97	12	116
85		$0.5 < R_e < 0.7$	$-0.3 < \Delta I_e < -0.1$	2.38	0.56	-0.13	2.49	26	152
86			$-0.1 < \Delta I_e < 0.1$	2.39	0.61	0.01	2.61	242	527
87			$0.1 < \Delta I_e < 0.3$	2.39	0.63	0.13	2.70	43	244
88		$0.7 < R_e < 0.9$	$-0.3 < \Delta I_e < -0.1$	...	...	...	...	3	50
89			$-0.1 < \Delta I_e < 0.1$	2.39	0.76	0.02	2.42	153	420
90			$0.1 < \Delta I_e < 0.3$	2.40	0.77	0.12	2.54	26	190

NOTE. —  $I_e$  is computed in the  $V$ -band.

\* Quoted values are in log units, i.e.,  $\log \sigma$ ,  $\log R_e$ , and  $\Delta \log I_e$ .

† Total number of galaxies in the stacked spectrum.

‡ Effective median  $S/N$  of the stacked spectrum.

TABLE 2  
LICK INDICES AND STELLAR POPULATION PROPERTIES OF STACKED SPECTRA

	H $\beta$ (Å)	(Fe) (Å)	Mg $b$ (Å)	Age $^\dagger$ (Gyr)	[Fe/H] (dex)	[Mg/H] (dex)	[Mg/Fe] (dex)
1	1.82 $\pm$ 0.08	2.11 $\pm$ 0.09	3.29 $\pm$ 0.08	10.3 $\pm$ 1.5	-0.48 $\pm$ 0.05	-0.22 $\pm$ 0.08	0.26 $\pm$ 0.06
2	2.00 $\pm$ 0.04	2.24 $\pm$ 0.05	3.10 $\pm$ 0.04	7.1 $\pm$ 0.5	-0.33 $\pm$ 0.03	-0.18 $\pm$ 0.03	0.15 $\pm$ 0.02
3	2.23 $\pm$ 0.06	2.50 $\pm$ 0.07	2.93 $\pm$ 0.06	4.1 $\pm$ 0.5	-0.09 $\pm$ 0.04	-0.06 $\pm$ 0.05	0.03 $\pm$ 0.03
4	1.81 $\pm$ 0.05	2.25 $\pm$ 0.05	3.21 $\pm$ 0.05	10.1 $\pm$ 0.9	-0.39 $\pm$ 0.03	-0.23 $\pm$ 0.03	0.16 $\pm$ 0.02
5	1.99 $\pm$ 0.03	2.40 $\pm$ 0.03	3.27 $\pm$ 0.03	6.9 $\pm$ 0.3	-0.22 $\pm$ 0.01	-0.10 $\pm$ 0.03	0.12 $\pm$ 0.02
6	2.20 $\pm$ 0.03	2.35 $\pm$ 0.04	3.02 $\pm$ 0.03	4.7 $\pm$ 0.3	-0.19 $\pm$ 0.02	-0.09 $\pm$ 0.03	0.10 $\pm$ 0.02
7	1.86 $\pm$ 0.05	2.36 $\pm$ 0.05	3.30 $\pm$ 0.04	8.9 $\pm$ 0.7	-0.29 $\pm$ 0.03	-0.15 $\pm$ 0.04	0.14 $\pm$ 0.03
8	2.07 $\pm$ 0.03	2.36 $\pm$ 0.03	3.27 $\pm$ 0.03	5.8 $\pm$ 0.3	-0.23 $\pm$ 0.02	-0.07 $\pm$ 0.03	0.16 $\pm$ 0.02
9	2.17 $\pm$ 0.05	2.37 $\pm$ 0.05	3.37 $\pm$ 0.04	4.9 $\pm$ 0.4	-0.17 $\pm$ 0.03	0.02 $\pm$ 0.04	0.18 $\pm$ 0.03
10	1.86 $\pm$ 0.09	2.48 $\pm$ 0.11	3.36 $\pm$ 0.09	8.8 $\pm$ 1.4	-0.22 $\pm$ 0.05	-0.14 $\pm$ 0.07	0.08 $\pm$ 0.05
11	1.96 $\pm$ 0.05	2.45 $\pm$ 0.06	3.55 $\pm$ 0.05	7.2 $\pm$ 0.6	-0.19 $\pm$ 0.03	-0.03 $\pm$ 0.04	0.16 $\pm$ 0.02
12	2.12 $\pm$ 0.08	2.27 $\pm$ 0.09	3.13 $\pm$ 0.08	5.4 $\pm$ 0.7	-0.26 $\pm$ 0.05	-0.09 $\pm$ 0.07	0.17 $\pm$ 0.05
13	... $\pm$ ...	... $\pm$ ...	... $\pm$ ...	... $\pm$ ...	... $\pm$ ...	... $\pm$ ...	... $\pm$ ...
14	1.78 $\pm$ 0.09	2.51 $\pm$ 0.11	3.40 $\pm$ 0.09	10.1 $\pm$ 1.6	-0.24 $\pm$ 0.05	-0.15 $\pm$ 0.07	0.09 $\pm$ 0.05
15	... $\pm$ ...	... $\pm$ ...	... $\pm$ ...	... $\pm$ ...	... $\pm$ ...	... $\pm$ ...	... $\pm$ ...
16	1.77 $\pm$ 0.06	2.49 $\pm$ 0.06	3.35 $\pm$ 0.06	10.4 $\pm$ 1.0	-0.26 $\pm$ 0.03	-0.18 $\pm$ 0.04	0.08 $\pm$ 0.03
17	1.92 $\pm$ 0.03	2.42 $\pm$ 0.03	3.31 $\pm$ 0.03	7.8 $\pm$ 0.4	-0.23 $\pm$ 0.02	-0.12 $\pm$ 0.03	0.12 $\pm$ 0.02
18	2.21 $\pm$ 0.04	2.46 $\pm$ 0.05	3.19 $\pm$ 0.04	4.5 $\pm$ 0.6	-0.11 $\pm$ 0.03	-0.02 $\pm$ 0.03	0.09 $\pm$ 0.02
19	1.83 $\pm$ 0.04	2.42 $\pm$ 0.04	3.56 $\pm$ 0.03	9.2 $\pm$ 0.6	-0.25 $\pm$ 0.02	-0.08 $\pm$ 0.03	0.17 $\pm$ 0.02
20	1.97 $\pm$ 0.02	2.47 $\pm$ 0.02	3.53 $\pm$ 0.02	6.9 $\pm$ 0.2	-0.16 $\pm$ 0.01	-0.01 $\pm$ 0.01	0.15 $\pm$ 0.01
21	2.13 $\pm$ 0.03	2.43 $\pm$ 0.04	3.42 $\pm$ 0.03	5.2 $\pm$ 0.3	-0.15 $\pm$ 0.02	0.01 $\pm$ 0.03	0.16 $\pm$ 0.02
22	1.82 $\pm$ 0.03	2.44 $\pm$ 0.04	3.41 $\pm$ 0.03	9.3 $\pm$ 0.6	-0.26 $\pm$ 0.02	-0.13 $\pm$ 0.03	0.13 $\pm$ 0.02
23	1.93 $\pm$ 0.02	2.49 $\pm$ 0.02	3.57 $\pm$ 0.02	7.4 $\pm$ 0.2	-0.17 $\pm$ 0.01	-0.02 $\pm$ 0.01	0.15 $\pm$ 0.01
24	2.10 $\pm$ 0.03	2.55 $\pm$ 0.04	3.49 $\pm$ 0.03	5.3 $\pm$ 0.3	-0.08 $\pm$ 0.02	0.05 $\pm$ 0.03	0.13 $\pm$ 0.02
25	1.83 $\pm$ 0.06	2.32 $\pm$ 0.07	3.44 $\pm$ 0.06	9.4 $\pm$ 1.1	-0.32 $\pm$ 0.04	-0.13 $\pm$ 0.06	0.19 $\pm$ 0.05
26	1.85 $\pm$ 0.03	2.51 $\pm$ 0.04	3.59 $\pm$ 0.03	8.6 $\pm$ 0.5	-0.19 $\pm$ 0.02	-0.05 $\pm$ 0.03	0.14 $\pm$ 0.02
27	2.14 $\pm$ 0.06	2.50 $\pm$ 0.07	3.53 $\pm$ 0.06	4.9 $\pm$ 0.6	-0.09 $\pm$ 0.04	0.07 $\pm$ 0.05	0.16 $\pm$ 0.03
28	1.96 $\pm$ 0.12	2.07 $\pm$ 0.15	3.28 $\pm$ 0.12	7.8 $\pm$ 1.6	-0.45 $\pm$ 0.09	-0.13 $\pm$ 0.12	0.32 $\pm$ 0.09
29	1.85 $\pm$ 0.09	2.57 $\pm$ 0.10	3.57 $\pm$ 0.08	8.6 $\pm$ 1.3	-0.16 $\pm$ 0.05	-0.04 $\pm$ 0.07	0.12 $\pm$ 0.05
30	... $\pm$ ...	... $\pm$ ...	... $\pm$ ...	... $\pm$ ...	... $\pm$ ...	... $\pm$ ...	... $\pm$ ...
31	1.73 $\pm$ 0.04	2.46 $\pm$ 0.04	3.66 $\pm$ 0.04	11.1 $\pm$ 0.8	-0.27 $\pm$ 0.02	-0.10 $\pm$ 0.03	0.17 $\pm$ 0.02
32	1.84 $\pm$ 0.02	2.49 $\pm$ 0.02	3.66 $\pm$ 0.02	8.7 $\pm$ 0.3	-0.20 $\pm$ 0.01	-0.04 $\pm$ 0.02	0.16 $\pm$ 0.02
33	2.04 $\pm$ 0.03	2.51 $\pm$ 0.03	3.51 $\pm$ 0.03	6.0 $\pm$ 0.4	-0.13 $\pm$ 0.02	0.01 $\pm$ 0.03	0.14 $\pm$ 0.02
34	1.80 $\pm$ 0.03	2.45 $\pm$ 0.03	3.79 $\pm$ 0.03	9.5 $\pm$ 0.5	-0.23 $\pm$ 0.02	-0.02 $\pm$ 0.03	0.21 $\pm$ 0.02
35	1.86 $\pm$ 0.01	2.56 $\pm$ 0.01	3.79 $\pm$ 0.01	8.3 $\pm$ 0.2	-0.14 $\pm$ 0.01	0.03 $\pm$ 0.01	0.17 $\pm$ 0.01
36	2.06 $\pm$ 0.02	2.61 $\pm$ 0.02	3.58 $\pm$ 0.02	5.5 $\pm$ 0.2	-0.05 $\pm$ 0.01	0.07 $\pm$ 0.02	0.12 $\pm$ 0.01
37	1.74 $\pm$ 0.03	2.47 $\pm$ 0.03	3.85 $\pm$ 0.03	10.6 $\pm$ 0.5	-0.24 $\pm$ 0.02	-0.03 $\pm$ 0.03	0.21 $\pm$ 0.02
38	1.84 $\pm$ 0.01	2.57 $\pm$ 0.01	3.86 $\pm$ 0.01	8.5 $\pm$ 0.2	-0.13 $\pm$ 0.01	0.05 $\pm$ 0.01	0.18 $\pm$ 0.01
39	2.04 $\pm$ 0.02	2.60 $\pm$ 0.02	3.60 $\pm$ 0.02	5.8 $\pm$ 0.3	-0.06 $\pm$ 0.01	0.06 $\pm$ 0.02	0.13 $\pm$ 0.01
40	1.76 $\pm$ 0.04	2.37 $\pm$ 0.05	3.67 $\pm$ 0.04	10.6 $\pm$ 0.8	-0.31 $\pm$ 0.03	-0.08 $\pm$ 0.04	0.23 $\pm$ 0.03
41	1.81 $\pm$ 0.02	2.58 $\pm$ 0.02	3.84 $\pm$ 0.02	9.1 $\pm$ 0.3	-0.15 $\pm$ 0.01	0.02 $\pm$ 0.01	0.17 $\pm$ 0.01
42	1.99 $\pm$ 0.03	2.65 $\pm$ 0.03	3.68 $\pm$ 0.03	6.4 $\pm$ 0.5	-0.04 $\pm$ 0.02	0.07 $\pm$ 0.03	0.11 $\pm$ 0.02
43	1.89 $\pm$ 0.11	2.23 $\pm$ 0.13	3.59 $\pm$ 0.11	8.5 $\pm$ 1.6	-0.34 $\pm$ 0.07	-0.06 $\pm$ 0.09	0.28 $\pm$ 0.06
44	1.72 $\pm$ 0.04	2.59 $\pm$ 0.05	3.89 $\pm$ 0.04	10.7 $\pm$ 0.8	-0.18 $\pm$ 0.02	-0.01 $\pm$ 0.03	0.17 $\pm$ 0.02
45	1.84 $\pm$ 0.05	2.67 $\pm$ 0.06	3.91 $\pm$ 0.05	8.3 $\pm$ 0.8	-0.07 $\pm$ 0.03	0.08 $\pm$ 0.04	0.15 $\pm$ 0.03
46	1.56 $\pm$ 0.04	2.46 $\pm$ 0.05	4.00 $\pm$ 0.04	15.2 $\pm$ 1.7	-0.19 $\pm$ 0.04	0.07 $\pm$ 0.04	0.26 $\pm$ 0.02
47	1.75 $\pm$ 0.02	2.46 $\pm$ 0.02	3.96 $\pm$ 0.02	10.2 $\pm$ 0.4	-0.23 $\pm$ 0.01	0.02 $\pm$ 0.02	0.25 $\pm$ 0.02
48	1.92 $\pm$ 0.03	2.61 $\pm$ 0.04	3.90 $\pm$ 0.03	7.3 $\pm$ 0.5	-0.08 $\pm$ 0.02	0.10 $\pm$ 0.03	0.18 $\pm$ 0.02
49	1.69 $\pm$ 0.03	2.48 $\pm$ 0.03	3.99 $\pm$ 0.02	11.4 $\pm$ 0.5	-0.25 $\pm$ 0.01	0.01 $\pm$ 0.03	0.26 $\pm$ 0.03
50	1.78 $\pm$ 0.01	2.61 $\pm$ 0.01	4.08 $\pm$ 0.01	9.4 $\pm$ 0.2	-0.12 $\pm$ 0.01	0.08 $\pm$ 0.01	0.21 $\pm$ 0.01
51	1.97 $\pm$ 0.02	2.67 $\pm$ 0.02	3.85 $\pm$ 0.02	6.6 $\pm$ 0.2	-0.02 $\pm$ 0.01	0.12 $\pm$ 0.01	0.14 $\pm$ 0.01
52	1.75 $\pm$ 0.03	2.50 $\pm$ 0.03	4.13 $\pm$ 0.02	10.2 $\pm$ 0.5	-0.20 $\pm$ 0.01	0.07 $\pm$ 0.03	0.27 $\pm$ 0.02
53	1.76 $\pm$ 0.01	2.65 $\pm$ 0.01	4.10 $\pm$ 0.01	9.6 $\pm$ 0.2	-0.11 $\pm$ 0.01	0.08 $\pm$ 0.02	0.19 $\pm$ 0.02
54	1.94 $\pm$ 0.02	2.67 $\pm$ 0.02	3.91 $\pm$ 0.01	7.0 $\pm$ 0.2	-0.03 $\pm$ 0.01	0.13 $\pm$ 0.02	0.16 $\pm$ 0.02
55	1.75 $\pm$ 0.04	2.42 $\pm$ 0.04	4.20 $\pm$ 0.04	10.4 $\pm$ 0.7	-0.24 $\pm$ 0.02	0.08 $\pm$ 0.03	0.32 $\pm$ 0.02
56	1.77 $\pm$ 0.01	2.66 $\pm$ 0.01	4.06 $\pm$ 0.01	9.4 $\pm$ 0.2	-0.10 $\pm$ 0.01	0.08 $\pm$ 0.01	0.18 $\pm$ 0.01
57	1.90 $\pm$ 0.02	2.63 $\pm$ 0.02	3.91 $\pm$ 0.02	7.5 $\pm$ 0.3	-0.07 $\pm$ 0.01	0.10 $\pm$ 0.02	0.17 $\pm$ 0.01
58	1.77 $\pm$ 0.07	2.34 $\pm$ 0.08	4.15 $\pm$ 0.07	10.1 $\pm$ 1.3	-0.29 $\pm$ 0.04	0.07 $\pm$ 0.06	0.36 $\pm$ 0.05
59	1.70 $\pm$ 0.02	2.62 $\pm$ 0.03	4.05 $\pm$ 0.02	10.9 $\pm$ 0.5	-0.16 $\pm$ 0.01	0.03 $\pm$ 0.02	0.19 $\pm$ 0.02
60	1.83 $\pm$ 0.04	2.57 $\pm$ 0.04	4.05 $\pm$ 0.04	8.5 $\pm$ 0.6	-0.12 $\pm$ 0.02	0.11 $\pm$ 0.03	0.23 $\pm$ 0.02
61	1.59 $\pm$ 0.05	2.44 $\pm$ 0.06	4.35 $\pm$ 0.05	13.8 $\pm$ 1.3	-0.28 $\pm$ 0.03	0.05 $\pm$ 0.05	0.33 $\pm$ 0.04
62	1.65 $\pm$ 0.03	2.59 $\pm$ 0.03	4.40 $\pm$ 0.03	11.8 $\pm$ 0.6	-0.17 $\pm$ 0.02	0.11 $\pm$ 0.03	0.28 $\pm$ 0.02
63	1.76 $\pm$ 0.07	2.73 $\pm$ 0.09	4.25 $\pm$ 0.07	9.3 $\pm$ 1.1	-0.05 $\pm$ 0.04	0.14 $\pm$ 0.06	0.19 $\pm$ 0.05
64	1.60 $\pm$ 0.03	2.59 $\pm$ 0.04	4.32 $\pm$ 0.03	12.9 $\pm$ 0.7	-0.19 $\pm$ 0.02	0.07 $\pm$ 0.03	0.26 $\pm$ 0.02
65	1.66 $\pm$ 0.02	2.61 $\pm$ 0.02	4.40 $\pm$ 0.02	11.4 $\pm$ 0.3	-0.15 $\pm$ 0.01	0.13 $\pm$ 0.01	0.28 $\pm$ 0.01
66	1.82 $\pm$ 0.03	2.79 $\pm$ 0.04	4.19 $\pm$ 0.03	8.4 $\pm$ 0.5	0.01 $\pm$ 0.01	0.17 $\pm$ 0.03	0.16 $\pm$ 0.02
67	1.58 $\pm$ 0.03	2.59 $\pm$ 0.03	4.44 $\pm$ 0.03	13.3 $\pm$ 0.7	-0.19 $\pm$ 0.02	0.09 $\pm$ 0.03	0.28 $\pm$ 0.02
68	1.70 $\pm$ 0.01	2.69 $\pm$ 0.01	4.34 $\pm$ 0.01	10.5 $\pm$ 0.2	-0.09 $\pm$ 0.01	0.14 $\pm$ 0.01	0.23 $\pm$ 0.01
69	1.88 $\pm$ 0.02	2.73 $\pm$ 0.02	4.13 $\pm$ 0.02	7.5 $\pm$ 0.3	-0.00 $\pm$ 0.01	0.18 $\pm$ 0.02	0.18 $\pm$ 0.02
70	1.60 $\pm$ 0.04	2.58 $\pm$ 0.04	4.47 $\pm$ 0.04	12.9 $\pm$ 0.9	-0.19 $\pm$ 0.02	0.11 $\pm$ 0.03	0.30 $\pm$ 0.02
71	1.69 $\pm$ 0.01	2.69 $\pm$ 0.01	4.39 $\pm$ 0.01	10.7 $\pm$ 0.2	-0.10 $\pm$ 0.01	0.14 $\pm$ 0.02	0.24 $\pm$ 0.02
72	1.87 $\pm$ 0.02	2.76 $\pm$ 0.02	4.20 $\pm$ 0.02	7.6 $\pm$ 0.2	0.01 $\pm$ 0.01	0.19 $\pm$ 0.01	0.18 $\pm$ 0.01
73	1.60 $\pm$ 0.08	2.46 $\pm$ 0.09	4.68 $\pm$ 0.07	13.1 $\pm$ 1.8	-0.24 $\pm$ 0.05	0.17 $\pm$ 0.08	0.41 $\pm$ 0.06
74	1.65 $\pm$ 0.02	2.67 $\pm$ 0.02	4.35 $\pm$ 0.02	11.5 $\pm$ 0.3	-0.12 $\pm$ 0.01	0.11 $\pm$ 0.02	0.24 $\pm$ 0.02



TABLE 2  
LICK INDICES AND STELLAR POPULATION PROPERTIES OF STACKED SPECTRA

75	$1.84 \pm 0.02$	$2.74 \pm 0.03$	$3.22 \pm 0.02$	$8.2 \pm 0.4$	$-0.05 \pm 0.01$	$0.03 \pm 0.82$	$0.08 \pm 0.82$
76	$1.47 \pm 0.08$	$2.50 \pm 0.10$	$4.59 \pm 0.08$	$\dots \pm \dots^\dagger$	$-0.19 \pm 0.06$	$0.20 \pm 0.08$	$0.38 \pm 0.05$
77	$1.62 \pm 0.04$	$2.71 \pm 0.05$	$4.58 \pm 0.04$	$11.8 \pm 0.8$	$-0.09 \pm 0.03$	$0.18 \pm 0.04$	$0.27 \pm 0.03$
78	$\dots \pm \dots$	$\dots \pm \dots$	$\dots \pm \dots$	$\dots \pm \dots$	$\dots \pm \dots$	$\dots \pm \dots$	$\dots \pm \dots$
79	$1.53 \pm 0.05$	$2.68 \pm 0.06$	$4.72 \pm 0.05$	$14.0 \pm 1.4$	$-0.14 \pm 0.03$	$0.16 \pm 0.05$	$0.30 \pm 0.04$
80	$1.62 \pm 0.03$	$2.75 \pm 0.03$	$4.60 \pm 0.03$	$11.7 \pm 0.5$	$-0.07 \pm 0.02$	$0.19 \pm 0.03$	$0.26 \pm 0.03$
81	$\dots \pm \dots$	$\dots \pm \dots$	$\dots \pm \dots$	$\dots \pm \dots$	$\dots \pm \dots$	$\dots \pm \dots$	$\dots \pm \dots$
82	$1.55 \pm 0.04$	$2.55 \pm 0.05$	$4.67 \pm 0.04$	$13.7 \pm 1.1$	$-0.20 \pm 0.03$	$0.17 \pm 0.04$	$0.37 \pm 0.04$
83	$1.58 \pm 0.02$	$2.74 \pm 0.02$	$4.67 \pm 0.02$	$12.4 \pm 0.3$	$-0.09 \pm 0.01$	$0.19 \pm 0.01$	$0.28 \pm 0.01$
84	$1.79 \pm 0.07$	$2.87 \pm 0.08$	$4.60 \pm 0.06$	$8.4 \pm 1.0$	$0.05 \pm 0.03$	$0.27 \pm 0.04$	$0.22 \pm 0.03$
85	$1.55 \pm 0.05$	$2.66 \pm 0.05$	$4.63 \pm 0.05$	$13.5 \pm 1.2$	$-0.15 \pm 0.03$	$0.15 \pm 0.04$	$0.30 \pm 0.02$
86	$1.63 \pm 0.01$	$2.76 \pm 0.02$	$4.57 \pm 0.01$	$11.5 \pm 0.3$	$-0.06 \pm 0.01$	$0.19 \pm 0.01$	$0.25 \pm 0.01$
87	$1.71 \pm 0.03$	$2.80 \pm 0.03$	$4.47 \pm 0.03$	$9.9 \pm 0.5$	$-0.02 \pm 0.02$	$0.19 \pm 0.03$	$0.21 \pm 0.02$
88	$\dots \pm \dots$	$\dots \pm \dots$	$\dots \pm \dots$	$\dots \pm \dots$	$\dots \pm \dots$	$\dots \pm \dots$	$\dots \pm \dots$
89	$1.60 \pm 0.02$	$2.80 \pm 0.02$	$4.64 \pm 0.02$	$11.9 \pm 0.3$	$-0.05 \pm 0.01$	$0.20 \pm 0.01$	$0.25 \pm 0.01$
90	$1.74 \pm 0.04$	$2.83 \pm 0.04$	$4.36 \pm 0.03$	$9.4 \pm 0.6$	$0.01 \pm 0.01$	$0.19 \pm 0.03$	$0.18 \pm 0.02$

---

NOTE. —  $\dagger$  Ages are determined from  $H\beta$  for all stacked spectra with the exception of spectrum 76, whose weak  $H\beta$  absorption falls outside the parameter space covered by the models. For this index,  $H\gamma_F$  is used in the fitting process to determine abundances. For consistency, the age measured for this spectrum is not used in the analysis here, as ages derived from  $H\gamma_F$  are typically somewhat younger than those derived from  $H\beta$  (see Graves & Schiavon 2008).